Structures of radial spokes and associated complexes important for ciliary motility

Miao Gui[1], **Meisheng Ma**[2], **Erica Sze-Tu**[1], **Xiangli Wang**[2], **Fujiet Koh**[1,3], **Ellen D. Zhong**[4,5], **Bonnie Berger**[5,6], **Joseph H. Davis**[4,7], **Susan K. Dutcher**[8], **Rui Zhang**[2,*], **Alan Brown**[1,*]

[1]Department of Biological Chemistry and Molecular Pharmacology, Blavatnik Institute, Harvard Medical School, 240 Longwood Avenue, Boston, MA, USA [2]Department of Biochemistry and Molecular Biophysics, Washington University in St. Louis, School of Medicine, St. Louis, MO, USA [3]Current address: Thermo Fisher Scientific, Eindhoven, Netherlands [4]Computational and Systems Biology, Massachusetts Institute of Technology, Cambridge, MA, USA [5]Computer Science and Artificial Intelligence Laboratory, Massachusetts Institute of Technology, Cambridge, MA, USA [6]Department of Mathematics, Massachusetts Institute of Technology, Cambridge, MA, USA [7]Department of Biology, Massachusetts Institute of Technology, Cambridge, MA, USA [8]Department of Genetics, Washington University in St. Louis, St Louis, MO, USA

Abstract

In motile cilia, a mechanoregulatory network is responsible for converting the action of thousands of dynein motors bound to doublet microtubules into a single propulsive waveform. Here, we use two complementary cryo-EM strategies to determine structures of the major mechanoregulators that bind ciliary doublet microtubules in *Chlamydomonas reinhardtii*. We determine structures of isolated radial spoke RS1, and the microtubule-bound RS1, RS2, and the nexin-dynein regulatory complex. From these structures, we identify and build atomic models for 30 proteins including 23 radial-spoke subunits. We reveal how mechanoregulatory complexes dock to doublet microtubules with regular 96-nm periodicity and communicate with one another. Additionally, we observe a direct and dynamically coupled association between RS2 and the dynein motor IDA*c*, providing a molecular basis for the control of motor activity by mechanical signals. These structures advance our understanding of the role of mechanoregulation in defining the ciliary waveform.

Motile cilia (also known as flagella) beat rhythmically to produce a driving force for locomotion or fluid flow depending on whether the cell is free to move or not. Single-cell eukaryotes, like the model organism *Chlamydomonas reinhardtii* and the pathogens that cause malaria, trypanosomiasis and giardiasis, use their flagella for swimming, mating, host

invasion, survival, and pathology[1]. In multicellular organisms, most ciliated cells, with the notable exception of spermatozoa, are not free swimming but instead line epithelial surfaces and generate fluid flow by producing metachronal waves. In humans, cilia-driven fluid flow clears the airways of trapped pathogens[2], assists in the transport of the egg to the uterus[3], circulates cerebrospinal fluid in the brain[4], and determines the left-right axis of the body plane in the embryonic node[5].

Central to all motile cilia is the axoneme, a highly patterned geometric arrangement of microtubules, dynein motors and mechanoregulatory complexes[6]. The axoneme of most motile cilia consists of nine doublet microtubules arranged in a circle around a central pair (CP) of singlet microtubules (Fig. 1a). Attached to the doublet microtubules are two rows of dynein motors, the outer dynein arms (ODAs) and the inner dynein arms (IDAs), with complementary functions. The ODAs provide much of the power output, whereas the IDAs define the waveform[7]. The regular beating pattern of cilia requires the spatial and temporal inhibition of these dynein motors[8] by a mechanical feedback loop that involves the CP and mechanoregulatory complexes that are periodically bound to doublet microtubules called radial spokes and the nexin-dynein regulatory complex (N-DRC). The N-DRC converts the action of the dynein motors into microtubule bending[9,10] and radial spokes ensure the dyneins function together to form a regular waveform[11,12]. In the absence of radial spokes, cilia are either paralyzed or have an irregular beat despite having active dynein.

The arrangement of these mechanoregulatory complexes within the axoneme has been characterized at nanometer resolution by electron cryotomography (cryo-ET) and subtomogram averaging[9,13–15]. Radial spokes are 40-nm long T-shaped complexes that repeat in pairs or triplets within the 96-nm repeat of the axoneme depending on the organism. Each radial spoke can be conceptually divided into a microtubule-associated base, a narrow stalk, a V-shaped neck, and a distal spokehead. In the model organism *Chlamydomonas reinhardtii*, there are two full-length radial spokes (RS1 and RS2) separated by 32 nm, and a shorter complex (RS3S) that binds 24 nm from RS2. The N-DRC occupies a site between RS2 and RS3S[9]. The exact composition of these complexes is unknown, with 11 N-DRC subunits[10,16] and at least 20 radial spoke proteins (RSPs)[17–19] described. High-resolution structural information is required to reveal the individual components, the detailed organization, and molecular mechanisms of this mechanoregulatory network, and to understand how mutations within mechanoregulators cause ciliopathies including primary ciliary dyskinesia and male infertility[20].

Results

Structures of radial spokes on doublet microtubules

We previously determined the structure of a doublet microtubule from *Chlamydomonas* by single-particle cryo-EM[21]. Although the doublet microtubules copurified with attached radial spokes and the N-DRC (Extended Data Fig. 1a), density for these complexes were largely absent from the final reconstruction due to on-doublet flexibility.

To overcome this flexibility, we developed a processing strategy (Extended Data Fig. 1) that allowed us to obtain on-doublet structures to various resolutions of RS1, RS2, RS3S, N-

DRC, IDA subform *c* (IDA*c*), and the CCDC39/40 coiled coil (Fig. 1b, Extended Data Figs. 2–3 and Table 1). The maps were of sufficient quality to build atomic models for the microtubule-associated regions of all complexes except RS3S (Extended Data Fig. 4, Table 1, and Supplementary Tables 1–2). As described later, a separate strategy was used to determine the structure of the radial spokehead (Fig. 1c). The combination of these two strategies provides a near-complete atomic model of radial spokes and their associated complexes attached to doublet microtubules (Fig. 1d).

Periodic docking of mechanoregulators to doublet microtubules

Previous structural and genetic studies had demonstrated that CCDC39/40 guides the placement of radial spokes along doublet microtubules[21–23] but how was not clear. Our structures show that the strict 96-nm periodicity and regular 32-nm spacing of the two radial spokes are determined by molecular adaptors that "read" the sequence of the CCDC39/40 coiled coil at the base of each radial spoke (Fig. 2a). For RS1, this adaptor is FAP253 and for RS2 it is FAP91. Consistent with each spoke having a different adaptor, microRNA-mediated knockdown of FAP91 leads to the selective loss of RS2[24]. Despite their functional equivalence, FAP91 and FAP253 bind differently to CCDC39/40. FAP253 interacts through a small interface dominated by salt bridges (Fig. 2b,c), whereas FAP91 forms an extended, hydrophobic triple helix with CCDC39/40 (Fig. 2d). The docking mechanism for the N-DRC is more complicated and involves FAP91, a heterodimer of DRC1 and DRC2 and a homodimer of DRC4 (Fig. 2a, Extended Data Fig. 4c). However, the principle of reading specific sequences within the CCDC39/40 coiled coil is the same. As FAP91 spans the 12-nm length between RS2 and the N-DRC and is also proposed to connect RS2 and RS3S as part of the calmodulin and spoke-associated complex (CSC)[25], it occupies, together with CCDC39/40, a privileged position to relay signals between mechanoregulators. The N-DRC is connected to the ODAs via the outer–inner dynein linkers[26], generating a network by which mechanoregulatory signals from the radial spokes could be propagated throughout the axoneme.

Our on-doublet structures show that RS1 and RS2 have identical spokeheads (Extended Data Fig. 1d) but differ in the composition and copy numbers of subunits in their stalks (Supplementary Table 2). The stalk of RS1 contains four homodimers of LC8 (RSP22) and a single copy of an armadillo repeat protein, RSP14 (Fig. 1b). In contrast, the stalk of RS2 has an appendage of two additional LC8 homodimers, a curved leucine-rich-repeat protein that we identify as RSP15, and RSP8, a structural homolog of RSP14 (Fig. 1b). Even FAP207, which is present in both stalks and acts as a microtubule-binding strut, has distinct structural arrangements and interacts with different protofilaments: A02 for RS1 and A03 for RS2 (Fig. 2e,f). The unique compositions of the stalks explain the gross morphological differences seen by cryo-ET[13,14].

Structure and assembly of a radial spoke

Neither spokehead could be resolved beyond 4.6 Å resolution using our on-doublet strategy (Extended Data Fig. 2a). To generate maps sufficient for model building, we therefore salt-stripped radial spokes from doublet microtubules and imaged them separately (Fig. 1a, Extended Data Fig. 5). This strategy resolved the structure of a complete radial spoke to 3.2–

3.7 Å resolution (Fig. 1c, Extended Data Fig. 6), allowing modeling of the spokehead and neck (Fig. 1d, Table 1, and Supplementary Tables 1–2). Unexpectedly, comparison of the structure with the on-doublet stalks revealed that the isolated radial spoke corresponded to RS1 only (Extended Data Fig. 7). The electrostatic docking mechanism for RS1 (Fig. 2c) may explain its selective extraction by high salt. Consistent with RS1 being stripped more easily from doublet microtubules than RS2, *in silico* analysis revealed that ~30% of doublet microtubule particles that have RS2 lack RS1 (Extended Data Fig. 1).

The spokehead consists of two symmetric lobes, as shown at lower resolution by cryo-ET[13] and single-particle cryo-EM[27]. Each lobe contains an RSP9 homodimer, heterodimers of RSP4/RSP6 and RSP2/RSP23, and single copies of RSP1, RSP3, RSP5, and RSP10 (Fig. 3a). The two lobes are dimerized exclusively through a homodimer of RSP16, a member of the HSP40 family of chaperones[28] (Fig. 3b). Spokehead dimerization is apparently important for waveform formation as RSP16 knockdown causes abnormal motility in *Chlamydomonas*[29] and mutations in its human ortholog are associated with ciliopathies[30] (Supplementary Table 3).

Within the axoneme, the spokeheads interact with the repetitive projections of the CP[31,32]. The spokehead surface that faces these projections is flat, slightly concave and remarkably electronegative, especially at its core (Fig. 3c). This unexpected charge distribution suggests a model where electrostatics govern the interactions between radial spokes and the CP.

As the spokeheads of RS1 and RS2 are identical[13] (Extended Data Fig. 1d), isolated RS1 also describes the spokehead of RS2. Docking the model into the subtomogram average of the *Chlamydomonas* axoneme (EMD-6872)[33] reveals that the spokeheads of RS1 and RS2 are connected by the distal β-sandwich domains of RSP1 (Fig. 3d). This bridge could be resolved to ~6 Å resolution by focused refinement of the connection between RS1-RS2 in our on-doublet structures (Extended Data Fig. 1b). The distance between the centers of the two spokeheads matches the 32-nm spacing between their bases, ensuring that the stalks are parallel to one another and that the flat surface of the conjoined spokeheads is parallel to the microtubule surface (Fig. 1d). Tomograms of axonemes from other species[15] reveal that although interactions between spokeheads are universal, the pairings are organism specific. In humans, RS2 interacts with RS3 but not RS1. Consistent with this lack of interaction between RS1 and RS2, the human RSP1 ortholog (RSPH1) does not have the β-sandwich domains of *Chlamydomonas* RSP1.

Interactions between RSP3 and radial spoke proteins

Previous work has shown that most of the spokehead subunits (with the notable exception of RSP16) preassemble together in the cytoplasm[28,34–36], whereas the stalk proteins RSP8 and LC8 do not[35,36] (Supplementary Table 2). This physical separation suggests that the stalk and spokehead assemble independently and come together in the cilium (Extended Data Fig. 8). Our structural data here suggest that RSP3, which spans the entire 40-nm length of the radial spoke[37] and is present in the precursor[34,35], plays a key role in uniting the spokehead and stalk (Fig. 4).

The extended N-terminus of RSP3 interacts with multiple copies of the LC8 homodimers, as shown biochemically[36], through β-strand addition (Fig. 4b,c). The avidity provided by this multivalent association may provide the basis for the stability of the mature complex. Consistent with a role in radial-spoke assembly, RSP3 provides localization signals for a variety of homo- and heterodimers (including RSP7/RSP11, RSP2/RSP23, RSP4/RSP6, FAP385/FAP385) (Fig. 4a). Each dimer forms a four-helix bundle that recognizes amphipathic sequences within the long α-helix of RSP3. The four-helix bundle of RSP7/RSP11 belongs to the RIIa dimerization/docking domain family, first identified in regulatory subunits of cAMP-dependent protein kinase A (PKA), which may explain previous observations that PKA can bind radial spokes *in vitro*[38].

RS2 and IDA*c* are physically coupled

At the base of RS2 attached to FAP207 we identified density corresponding to the single-headed dynein, IDA*c* (Fig. 5a). Within this density, we could unambiguously place globular actin and p28 homodimer, both known auxiliary subunits of IDA*c*[39,40]. Additional α-helices within the density may correspond to the tail of the IDA*c* heavy chain, which crosslinks with p28[41].

Density resembling IDA*c* is also seen at the base of RS1 in the subtomogram average of the *Chlamydomonas* axoneme[33] (Fig. 5b,c). This density corresponds to IDA*a,* which like IDA*c* copurifies with p28[39] and actin[40]. Docking our atomic model of IDA*c* into the subtomogram average of IDA*a* shows that p28 of IDA*a* interacts with FAP253 and not with FAP207 (Fig. 5c,d). Thus, while IDA*a* and IDA*c* both directly bind radial spokes they have different attachment mechanisms.

Regulation by mechanical and chemical signals

Electron microscopy has shown that radial spokes tilt as the cilium bends[31]. In straight sections of the axoneme, the radial spokes are parallel to one another and perpendicular to the doublet microtubule, whereas in bent sections, their stalks are obliquely aligned with the microtubules. As this bend-dependent conformational change may be an important regulatory mechanism, we used a neural network (see Methods) to analyze the flexibility of isolated RS1. The neural network identified one major movement: a tilting of the spokehead at the neck by 17° relative to the stalk in the direction of the microtubule axis (Fig. 6a and Supplementary Movie 1). This same tilting motion (22°) was also identified by multi-body analysis, in which the stalk and spokehead were considered as separate bodies (Extended Data Fig. 9a). Multi-body analysis of the on-doublet RS1 and RS2 revealed that tilting of the spokehead remains a major motion even when the radial spokes are attached to doublet microtubules and each another (Extended Data Fig. 9b,c). Furthermore, we identified that both stalks tilt relative to the doublet microtubule surface by 5-10° in the same direction as the spokehead tilt (Fig. 6b and Extended Data Fig. 9d). Thus, radial spokes appear to have two hinges of motion: one at the neck and one at the base. Together, these could account for the maximum 33° tilt angle observed in bent regions of the cilium in electron micrographs[31]. Importantly, our analysis also reveals that movement of IDA*c* is coupled to the tilt of RS2 (Fig. 6b). The ability of radial spokes to tilt when bound to doublet microtubules, and the coupling of this movement to the dynein motors, potentially provides a mechanism whereby

changes in the orientation of radial spokes could alter the orientation and/or conformations of dynein motors.

We identify calmodulin (RSP20), a Ca^{2+}-responsive protein, at the proposed interface between RS1 and IDA*a* bound to an IQ motif of FAP253 (Fig. 5d and Extended Data Fig. 10a). Comparison to previous structures of calmodulin bound to IQ motifs[42,43] (Extended Data Fig. 10b,c) revealed that FAP253-bound calmodulin is an apo-state, consistent with our use of a calcium-selective chelator during purification. A Ca^{2+}-dependent conformational switch in the FAP253-bound calmodulin structure could therefore modulate ciliary motility by affecting the RS1-IDA*a* interaction. This may be one mechanism by which calcium can directly alter the waveform of isolated axonemes *in vitro*[44]. Other mechanisms, such as calcium regulation of the calmodulin-like LC4 subunit of the ODA, may directly affect dynein behavior[45].

Other chemical signals, including redox status[46] and cyclic nucleotides[47], are also proposed to regulate ciliary motility[48]. Two of the identified RSPs (FAP198 in the neck and RSP5 in the spokehead) are associated with redox sensitivity. RSP5 is a member of the aldo-keto reductase family of NAD(P)H-dependent oxidoreductases[49] and FAP198 has an N-terminal domain that resembles the redox-sensitive heme-binding domain of cytochrome b5 (Supplementary Fig. 1). However, our structures show that RSP5 has neither the substrate-binding pocket nor the conserved catalytic tetrad of functional aldo-keto reductases (Extended Data Fig. 10d) and that FAP198 occludes its own heme-binding pocket (Extended Data Fig. 10e). FAP198 also probably renders RSP12, a putative peptidyl-prolyl *cis-trans* isomerase, inactive (Extended Data Fig. 10f). We therefore conclude that FAP198, RSP5 and RSP12 play only structural roles in the mature radial spoke. The link between radial spokes and nucleotide-mediated regulation of ciliary motility is more evident. We identify two probable binding sites for nucleotides in the spokehead – in the cyclic-nucleotide-binding GAF domain of RSP2 and the conserved binding site of the nucleoside diphosphate kinase domain of RSP23. Both domains contain density consistent with nucleotide ligands although we cannot unambiguously identify the nucleotide present (Extended Data Fig. 10g,h). The ability to integrate chemical and mechanical cues may explain the complexity of radial spokes.

Discussion

From our structural information we propose a model for the mechanoregulation of ciliary motility (Fig. 6c). Consistent with the asymmetric nature of the dynein inhibition[8], we favor a model where the mechanoregulatory signal originates at the asymmetric CP and is communicated to the dynein arms through radial spokes[37,48,50]. We show that for IDA*c* this relay mechanism can be direct, and that changes in the tilt angle of radial spokes can change the orientation of the dynein tail (Fig. 6b). In this way, the radial spokes could act as mechanical levers to physically reposition the dynein motors away from neighboring doublet microtubules and therefore inhibit dynein activities during the ciliary beat. IDA*c* is particularly important for force production under viscous load[51], suggesting that the dynamics of the RS2-IDA*c* pair may be sensitive to physical stresses. Interestingly, we identify differences in how IDA*a* and IDA*c* dock to radial spokes (Fig. 5), suggesting that

even similar IDAs have distinct regulatory mechanisms as well as distinct mechanical properties[40].

How are signals relayed between the CP and radial spoke? In straight sections of the axoneme, the electronegative surfaces of the radial spokeheads face the projections of the CP. As the axoneme bends, it is expected that the CP projections move closer to and potentially collide with a subset of the spokeheads[37]. Although it has been proposed that this contact triggers the mechanical signal that is propagated through the radial spoke[37], a collision-based model does not explain our new finding that the spokehead is highly charged. We therefore propose that spokeheads and CP projections interact electrostatically. In this model, an increase in the electrostatic force with decreasing distance as the axoneme bends causes the radial spoke to tilt, and this tilt is the mechanosignal that is transmitted to the stalk-associated IDAs, the N-DRC, and ultimately the ODAs (Fig. 6c). Alternatively, the CP of *Chlamydomonas* is reported to rotate during ciliary beating[52–54], which would have the effect of changing the partner projection for each radial spokehead, potentially with corresponding changes in electrostatic forces. Confirmation of the role of electrostatics in ciliary motility will require high-resolution structures of CP projections and three-dimensional visualization of their interactions with radial spokes as the cilium bends.

In conclusion, we resolve the structures of some of the key regulators of ciliary motility in atomic detail. We identify and build models for 23 RSPs, 3 subunits of the N-DRC, 2 subunits of IDA*c*, and the CCDC39/40 molecular ruler (Supplementary Table 1). We discover the molecular identity of RSP15 and reveal that FAP91, FAP198, FAP207, FAP253, and FAP385 are *bona fide* RSPs. Many of these proteins including the novel RSPs are conserved across species – orthologs of RSP15 and FAP198 have been identified by mass spectrometry in radial spokes isolated from *Ciona intestinalis*[55] – and are associated with human ciliopathies (Supplementary Table 3). From our structural and dynamic information, we propose an "electrostatic" model of mechanoregulation which reconciles the electronegative spokeheads, the intrinsic ability of radial spokes to tilt, and the coupled movement of radial spokes and IDAs. In addition, we identify a pathway by which calcium could regulate the transmission of mechanosignals. Our structures represent a step forward in understanding the regulatory mechanisms of ciliary motility.

Methods

Chlamydomonas reinhardtii culture

We used wild-type *Chlamydomonas reinhardtii* cells (strain CC-125) as the source for doublet microtubules and wild-type *Chlamydomonas* cells (strain CC-1690) as the source from which to isolate radial spokes. Both strains were obtained from the Chlamydomonas Resource Center at the University of Minnesota.

For doublet microtubule preparation, *Chlamydomonas* cells were spread onto 5 Tris-Acetate-Phosphate (TAP) agar plates at a starting density of 8×10^6 cells/plate and grown for 2 days at 25°C to reach a final density of 1.28×10^8 cells/plate. Cells from the 5 plates were resuspended in 80 mL of M-N/5 medium[56] and incubated at 25°C for 2 h to allow flagellar assembly. For radial spoke preparation, *Chlamydomonas* cells (strain CC-1690)

were grown in TAP medium at room temperature for 4-5 days and were harvested before the 8th light hour of a 12 h/12 h light-dark cycle at a concentration of ~3-5 × 10^6 cells/mL.

Flagella isolation and radial spoke purification

Flagella were isolated following a modified version of a published protocol[57], as described in detail in Supplementary Note 1. Radial spoke purification from isolated flagella is also described in Supplementary Note 1.

Mass-spectrometry analysis

The fraction from the monoQ elution corresponding to RS1 was denatured with SDS-loading buffer and loaded onto a 4-20% precast polyacrylamide gel (Bio-Rad). The gel was run for 3 min and then silver stained. The band was cut and sent for mass spectrometry analysis at the Taplin Mass Spectrometry Facility at Harvard Medical School. The annotated mass spectrometry data are provided as Supplementary Data 1. Mass spectrometry analysis of the doublet microtubule sample is reported in[21].

Negative-stain microscopy

4 μl of purified RS1 at a concentration of 0.03 mg/mL was applied onto a glow discharged continuous carbon grid (Electron Microscopy Sciences, Inc.). After one minute of adsorption, the grid was blotted with filter paper to remove excess sample, immediately washed twice with 4 μl of 1.5% uranyl formate solution and incubated with 4 μl of 1.5% uranyl formate solution for an additional one minute. The grid was then further blotted with filter paper to remove the uranyl formate solution, air-dried at room temperature, and examined with a Tecnai T12 electron microscope (Thermo Fisher Scientific) equipped with an LaB6 filament and operated at 120-kV acceleration voltage, using a nominal magnification of 52,000× at a pixel size of 2.13 Å.

Images were recorded using a Gatan 4k × 4k CCD camera with an exposure of 20–30 e⁻/Å^2. The defocus for data acquisition was set to between −1 μm and −3 μm. RELION-3.0[58] was used for all image processing steps. Firstly, ~500 particles were picked manually and subjected to two-dimensional (2D) classification. Good classes were selected and used as references to automatically pick particles from all micrographs. 3,293 particles were picked from 54 micrographs and three rounds of reference-free 2D classification were performed to select good particles. These particles were used to generate an initial three-dimensional (3D) density map using RELION-3.0 and for a round of 3D refinement in which the initial model was used as a reference.

Cryo-EM sample preparation

Doublet microtubules.—Cryo-EM grids of doublet microtubules were prepared as described[21].

Isolated RS1.—Cryo-EM grids of isolated radial spokes were prepared using a Vitrobot Mark IV (Thermo Fisher Scientific). 3 μl of purified RS1 at a concentration between 0.50 mg/mL to 0.75 mg/mL was applied onto glow discharged C-flat holy carbon grids (R1.2/1.3, 400 mesh copper, Electron Microscopy Sciences) or Quantifoil holy carbon grids (R1.2/1.3,

400 mesh copper or gold, Quantifoil Micro Tools). The grids were blotted for 7 s with a blot force of 16 and 100% humidity before being plunged into liquid ethane cooled by liquid nitrogen.

Cryo-EM data collection

On-doublet complexes.—To improve the resolution of RS1 and RS2 bound to doublet microtubules from our previous report[21], we collected ~9,600 additional micrographs with the same imaging conditions. All data were collected using a 300 keV Titan Krios microscope equipped with a Cs-corrector (Thermo Fisher Scientific) and a BioQuantum Energy Filter (Gatan) at the Washington University in St. Louis Center for Cellular Imaging (WUCCI). All movies were recorded with a K2 Summit direct electron detector (Gatan) in counting mode, with an exposure rate of 8.5 electrons/pixel/s on the detector camera. The images were recorded at a nominal magnification of 81,000×, corresponding to a calibrated pixel size of 1.403 Å. A total exposure time of 9 s, corresponding to a total dose of 38.9 electrons/$Å^2$ on the specimen, was fractionated into 30 movie frames. A defocus range from −1.0 to −3.5 μm was set during data acquisition. The data were collected automatically using EPU software (Thermo Fisher Scientific).

Isolated RS1.—Images of purified RS1 were acquired on a Titan Krios microscope at the Harvard Cryo-EM Center for Structural Biology operating at an acceleration voltage of 300 kV and equipped with a BioQuantum K3 Imaging Filter (slit width 25 eV) and a K3 direct electron detector (Gatan). Images were recorded at a defocus range of −1 to −3.2 μm with a nominal magnification of 81,000×, corresponding to a calibrated pixel size of 1.09 Å. This pixel size was calibrated based on the density map of the on-doublet RS1 spokehead obtained from the Titan Krios at the WUCCI. Each image was dose-fractionated into 50 movie frames with a total exposure time of 2.5 s and a frame exposure time of 0.05 s, resulting in a total dose of ~60 electrons per $Å^2$. SerialEM was used for data collection[59].

Image processing

On-doublet complexes.—The data were initially processed following the scheme described in[21]. Briefly, segments of the doublet microtubules were first extracted as non-overlapping 8-nm particles and classified into six classes using *Class3D* in RELION-3.1. One class, corresponding to the 48-nm repeat of the doublet microtubule, was arbitrarily selected and further classified into two classes, with each class corresponding to one half of the 96-nm repeat. Particles from one of the classes (referred to as 96-nm particles) were used for further processing. In the next step, during particle re-extraction in RELION-3.1, the coordinates of the centers of the 96-nm particles were shifted so that the feature of interest (e.g. RS1 spokehead/stalk, RS2 spokehead/stalk, RSP1-RSP1 interface, RS3S, IDA*c,* or N-DRC baseplate/lobe) was centered in the 3D reconstruction from these particles (Extended Data Fig. 1b). When possible, a smaller box size (256 or 384 instead of 512 pixels) was used to speed up data processing. In total, ~202,000 center-shifted 96-nm particles, with the doublet microtubule signal subtracted, were used to compute the structure of various 96-nm repeat features (Table 1). This is approximately double the number of particles from our previous report[21]. Subsequent 3D classification was performed using *Class3D* in RELION 3.1 to select a more homogeneous subset of particles for further refinement. For the RS1 and

RS2 bases and N-DRC baseplate, the microtubule signal was helpful for image alignment and was therefore not subtracted from the raw particle images, and a customized soft-edged binary mask covering protofilaments A1-A3 was used during refinement. Following post-processing in RELION-3.1, all maps were resolved to between 3.4 and 6.3 Å except for the distal lobe of N-DRC and RS3S, which were resolved to 7.0 Å and 14.4 Å resolution, respectively (Extended Data Fig. 2a). Further refinement using polished particles did not improve the resolution or map quality.

To generate a composite map for model building and refinement, the maps of the RS2 stalk, IDA*c*, N-DRC baseplate and the microtubule protofilaments to which they are attached were aligned using the *fit in map* command in Chimera[60] by maximizing the overlapped density between these maps. These maps were then merged using the *vop maximum* command in Chimera. The 6.1 Å map of the proximal region of the RS1 stalk was not included in the composite map due to its lower resolution than surrounding maps.

Isolated RS1.—A total of 14,391 movie stacks were motion corrected and electron-dose weighted using MotionCor2[61]. The CTF parameters were estimated from the motion-corrected micrographs using CTFFIND4[62]. 12,331 micrographs were selected for further processing based on visual inspection of the micrographs and their corresponding power spectra. Particles were automatically selected using CrYOLO[63] or Laplacian-of-Gaussian picker implemented in RELION-3.0. All subsequent 2D and 3D analyses were performed using RELION-3.0 or RELION-3.1.

256,239 particles were selected after several rounds of 2D classification from 2,320,543 auto-picked particles. Since most 2D classes centered at the head of the radial spoke, we re-centered the particles using a similar strategy as in[64]. Another round of 2D classification was performed to check that re-centering had worked. The data were then subjected to 3D classification. The density map generated with the negative-stain data was low-pass filtered to 30 Å and used as the initial model. 221,836 particles were selected after 3D classification for 3D refinement. After refinement, CTF refinement and Bayesian polishing was performed, followed by another 3D refinement, yielding a 3.7 Å density "consensus" map (Extended Data Fig. 5g, left).

To further improve the density map, several rounds of multi-body refinement[65], signal subtraction, and re-centering were performed (Extended Data Fig. 5g). First, we did a multi-body refinement with two masks, one that covered the spokehead and one that covered the neck and stalk. Signal subtraction was then performed and the density corresponding to each body were re-centered and extracted with a smaller boxsize of 480 pixel instead of 560 pixel for the consensus refinement. Masks with a soft edge of 6 pixels surrounding the two bodies were used for both multi-body refinement and signal subtraction. The signal-subtracted particles were centered on projections of the mass center of the masks. Individual 3D refinements were then performed on the spokehead and the neck/stalk. Since the spokehead has two-fold rotational symmetry, C2 symmetry was imposed during refinement, yielding a 3.2 Å density map. To improve the density of the extended domains of the spokehead, we used symmetry expansion[66], subtracted the density of half of the spokehead, performed a 3D classification to select 311,578 good particles from the 443,672 symmetry-expanded

particles and applied local masks during refinement. To further improve the density for the globular N-terminal domain of RSP1, we did signal subtraction, and re-centered and extracted the RSP1 density with a smaller boxsize of 200 pixel. Refinement of the subtracted RSP1 density yielded a 3.6 Å density map.

For the neck and stalk, 3D classification with local mask on the neck was performed after refinement. Selected particles were used for subsequent refinement, with a local mask of the neck applied, yielding a 3.6 Å density map. A similar strategy was used to improve the lower part of the stalk.

The composite map for the complete isolated radial spoke was generated using the *vop maximum* command in Chimera, as described for the on-doublet complexes. Briefly, three improved maps within the local masks of each asymmetric unit were combined with the central part of the C2 map, constituting the spokehead map. The local maps for the neck and the lower part of the stalk were combined with the central part of the overall neck and stalk map, constituting the composite neck and stalk map. Then the two maps were aligned with the consensus map and combined, generating the complete density map of the isolated radial spoke.

Analysis of RS1 dynamics by deep neural networks

CryoDRGN v0.0.19[67] models were trained on single-particle images of isolated RS1 down-sampled to an image size of 256x256 (2.40625 Å/pix) with their corresponding poses assigned from a consensus reconstruction in RELION. All reconstructions used a 1024x3 (nodes/layer x layer) fully connected architecture for the encoder and decoder networks. The latent variable dimension was 10. Training was performed in minibatches of 8 images using the Adam optimizer and a learning rate of 0.0001. For particle filtering, the initial stack of 221,836 images was randomly split into two halves of 110,918 particles, which were then processed separately. A cryoDRGN model was trained on each half stack for 50 epochs. Based on an analysis of the latent space, an interactive lasso tool was used to select particles corresponding to the full complex, resulting in 55,110 and 53,976 particles for each half stack, respectively. Excluded regions in the latent space corresponded to component variability in the spokehead dimer and particle images with edge artifacts. The observed heterogeneity was reproducible across replicate runs with different training hyperparameters (not shown). For the final reconstruction, a cryoDRGN model was trained on 98,177 particle images from the filtered half stacks for 50 epochs. After training, a continuous trajectory depicting the spokehead tilting was produced by generating 10 structures along the first principle component of the latent space data manifold at equally spaced points between the 5th and 95th percentile PC1 values.

Analysis of radial spoke dynamics by multi-body analysis

On-doublet complexes.—RELION-3.1 was used to perform multi-body analysis[65]. To analyze the on-doublet movement between the spokehead and stalk regions of RS1/RS2, we started from a consensus refinement that was focused on the spokehead and used two generous masks that separately covered the spokehead and stalk. To analyze the movement between the stalk of RS1 and the doublet microtubule, we started from a consensus

refinement that focused on the stalk and used two masks covering the RS1 stalk and doublet microtubule. To analyze the movements between the stalk of RS2, IDA*c* and the doublet microtubule, we used three masks covering each different region. The results were analyzed using *relion_flex_analyse*. Movements from the top three eigenvectors were examined.

Isolated RS1.—After a consensus 3D refinement of isolated RS1, two masks were applied during multi-body analysis. One mask covered the spokehead and the other covered the neck and stalk. The results were analyzed using *relion_flex_analyse*. Movements from the top three eigenvectors were examined.

Model building

All model building was performed in Coot[68]. Model building of the proximal regions of the stalks used the on-doublet maps of RS1 (EMD-22480) and RS2 (EMD-22481). Model building of the neck and spokehead used the composite map of isolated RS1 (EMD-22475). Interpretation of the on-doublet microtubules maps started with fitting of the model of the *Chlamydomonas* doublet microtubule (PDB 6U42)[21]. An accurate model of the CCDC39/40 coiled coil was then built. The RSPs were identified within the maps using one or more of the following strategies: 1) manual fold recognition, 2) automated density-guided fold recognition, 3) secondary structure assignment, 4) *de novo* sequence assignment, 5) prior knowledge, and 6) bioinformatic prediction (see Supplementary Note 1 for details). How each protein was identified, and the accuracy and completeness of the resulting models are summarized in Supplementary Table 1. Flagellar associated proteins (FAPs) are numbered according to[69].

Refinement

Atomic models for individual subunits were refined during model building using real-space refinement in Coot with torsion, planar peptide and Ramachandran restraints applied[68]. After model building, the subunits were combined into three separate PDB files corresponding to: 1) isolated RS1 (PDB 7JTK), 2) on-doublet RS2 stalk/N-DRC baseplate/IDA*c* (PDB 7JU4), and 3) on-doublet RS1 stalk (PDB 7JTS). These atomic models were then refined into their corresponding composite maps using Phenix.real_space_refine v1.18.2-3874[70]. Secondary structure, Ramachandran and rotamer restraints were applied during refinement of the models of isolated RS1 (resolution cutoff 3.7 Å) and the on-doublet RS2 stalk/N-DRC baseplate/IDA*c* (resolution cutoff 4.1 Å). A round of manual model correction in Coot was performed between rounds of real-space refinement in Phenix. The final refinement was performed for two or three macro cycles with strategies of *minimization_global* and *local_grid_search*. The model of the on-doublet RS1 stalk was refined using rigid body fitting only in Phenix as the resolution of the map was 6.1 Å. The quality of the refined models was analyzed by MolProbity[71], with their statistics reported in Table 1.

Figures

Figures were generated using Chimera[60], ChimeraX[72] or PyMOL[73]. Maps colored by local resolution were generated using RELION 3.1[58].

Software used in the project by members of the Brown laboratory were installed and configured by SBGrid[74].

Further information on experimental design is available in the Nature Research Reporting Summary linked to this article.

Code Availability

Code used for the initial separation of singlet and doublet microtubules is available on request from Rui Zhang (zhangrui@wustl.edu).

Data availability

Composite cryo-EM maps and atomic models have been deposited in the Electron Microscopy Data Bank (EMDB) and wwPDB, respectively, with accession codes EMD-22475 and PDB 7KTK (isolated RS1); and EMD-22481 and PDB 7JU4 (on-doublet RS2 stalk/IDA*c*/N-DRC). Constituent maps, and the masks that were applied during reconstruction, are associated with these depositions as additional files. Cryo-EM maps have been deposited with accession codes EMD-22480 (on-doublet RS1 stalk), with associated atomic model PDB 7JTS; EMD-22482 (on-doublet RS1 spokehead); EMD-22483 (on-doublet RS2 spokehead), and EMD-22486 (on-doublet RSP1 dimer).

Extended Data

Extended Data Fig. 1 |. Data collection and processing for the on-doublet mechanoregulatory complexes.

a, Section of an electron micrograph showing radial spokes (marked with an asterisk) bound to a doublet microtubule in vitreous ice. **b**, Processing scheme used to generate reconstructions of mechanoregulatory complexes bound to doublet microtubules (DMT, gray). To resolve various structural features with 96-nm periodicity (RS1 spokehead/stalk, RS2 spokehead/stalk, RSP1-RSP1 interface, RS3S, IDA*c*, or N-DRC baseplate/lobe), it was

necessary to use a combination of tubulin signal subtraction (TSS), shifting the center (SC) of coordinates to the feature of interest, focused refinement (FR) and 3D classification without alignment (3C). When possible, the box size was reduced (RB) to 256 or 384 instead of 512 pixels to facilitate data processing. **c**, Angular distribution of the particle views used for reconstruction of on-doublet RS2. Similar distributions were obtained for on-doublet RS1. The height of the cylinders, colored from blue to red, represents the number of particles. The final density map of RS2 is shown in gray. **d**, Superimposition of the on-doublet RS1 and RS2 spokeheads confirms that they have identical structure.
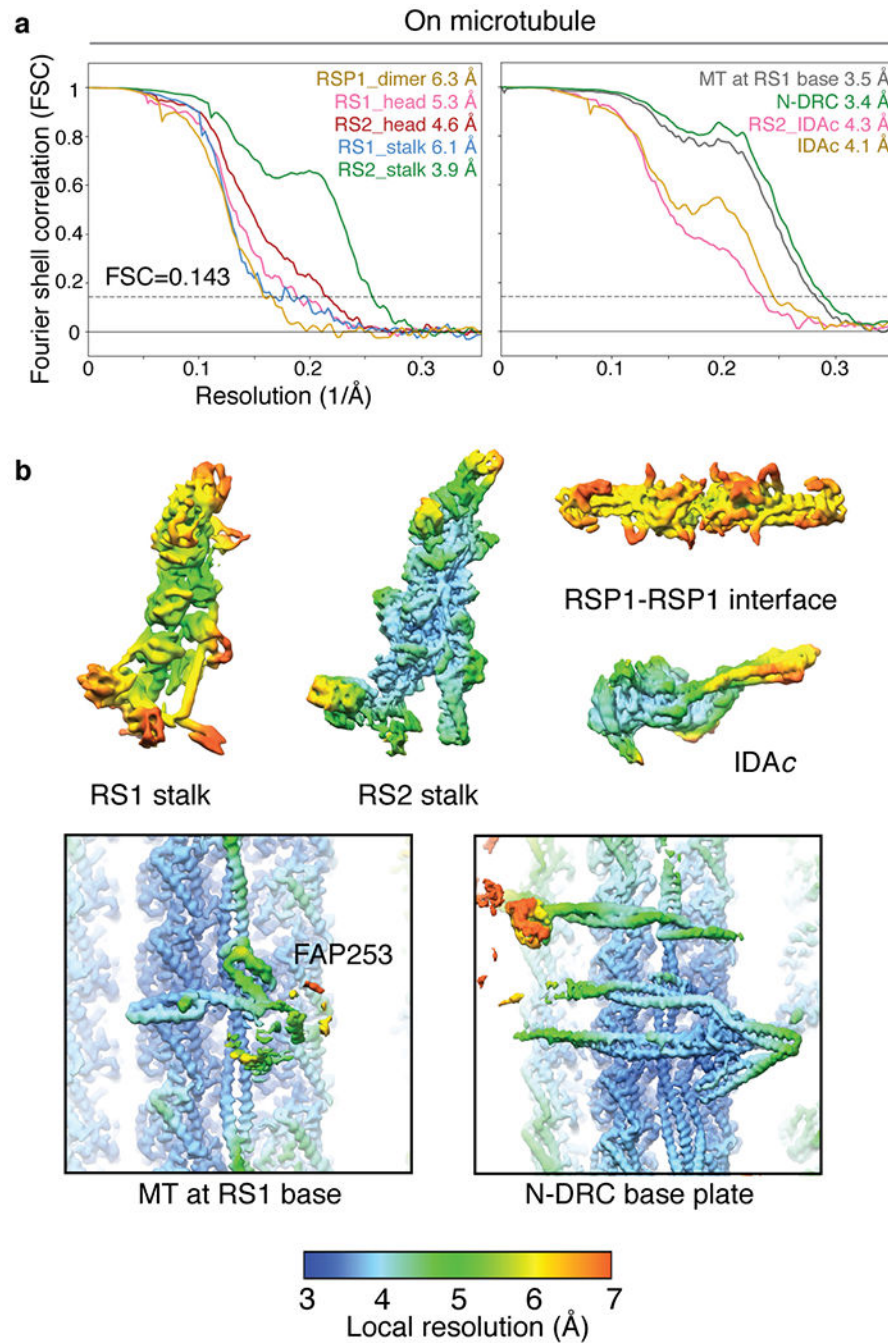
Extended Data Fig. 2 |. Global and local resolution of on-doublet mechanoregulatory complexes. **a**, Fourier shell correlation (FSC) curves calculated between masked independent half maps for on-doublet structures. Left panel, FSC curves are shown for focused refinements of the RS1 spokehead and stalk, RS2 spokehead and stalk, and the RSP1-RSP1 dimer. Right panel, FSC curves for the base of RS1, the RS2-IDA*c* complex, IDA*c*, and the N-DRC baseplate. The nominal resolution was estimated using the FSC = 0.143 criterion (dashed line). **b**, Density maps for on-doublet structures colored by local resolution. Only the maps used for model building are shown. The local resolution is colored from 3 to 7 Å.
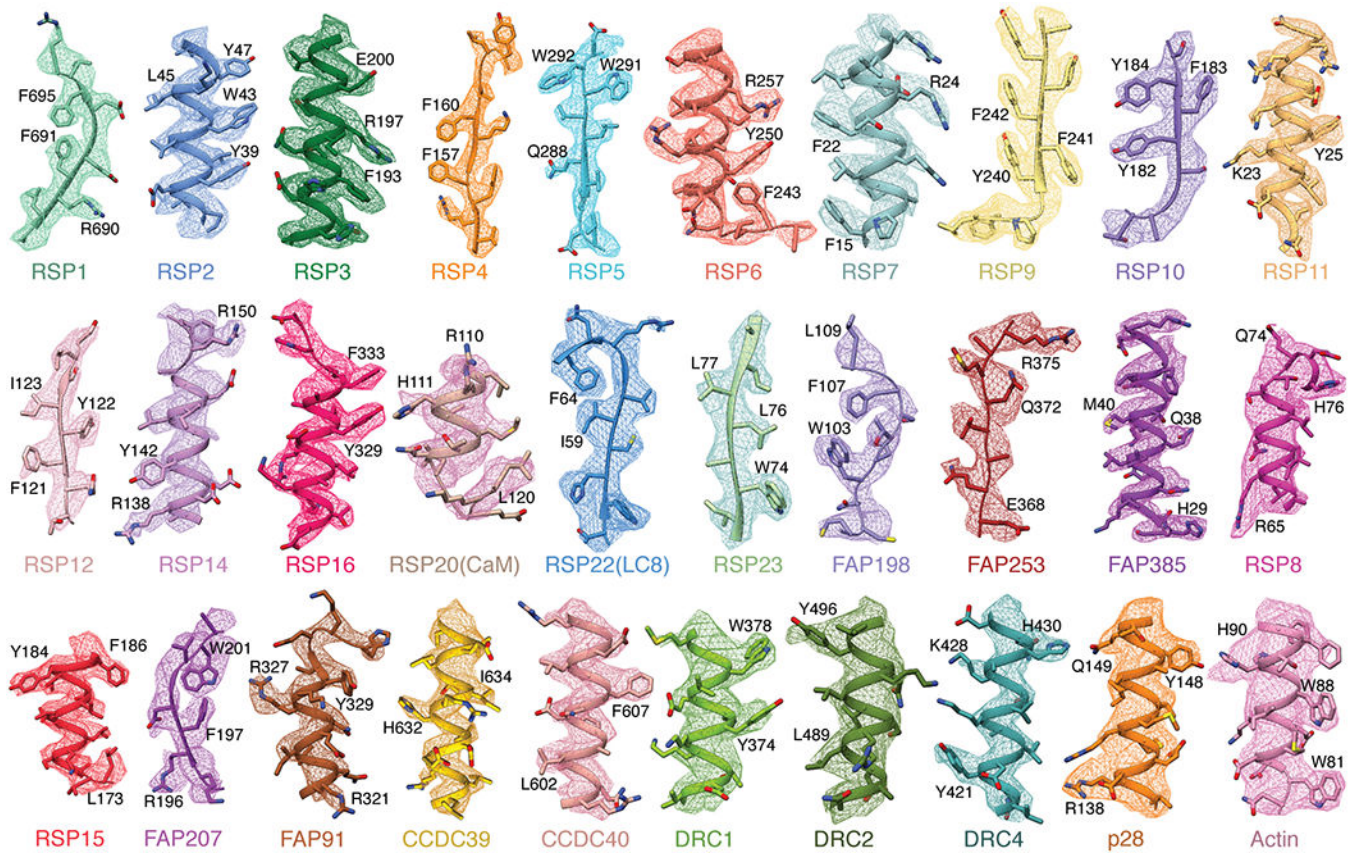
Extended Data Fig. 3 |. Map quality.

Examples of map density for all 30 non-tubulin proteins identified in this study. The first 19 proteins show density from isolated RS1 contoured at 0.009-0.013. The remaining 11 proteins (starting from RSP8) show density from on-doublet maps contoured at 0.020-0.031. Landmark residues are labeled. Note that the sidechains of RSP20 (calmodulin) and RSP8 are not well resolved and are truncated in the deposited model.
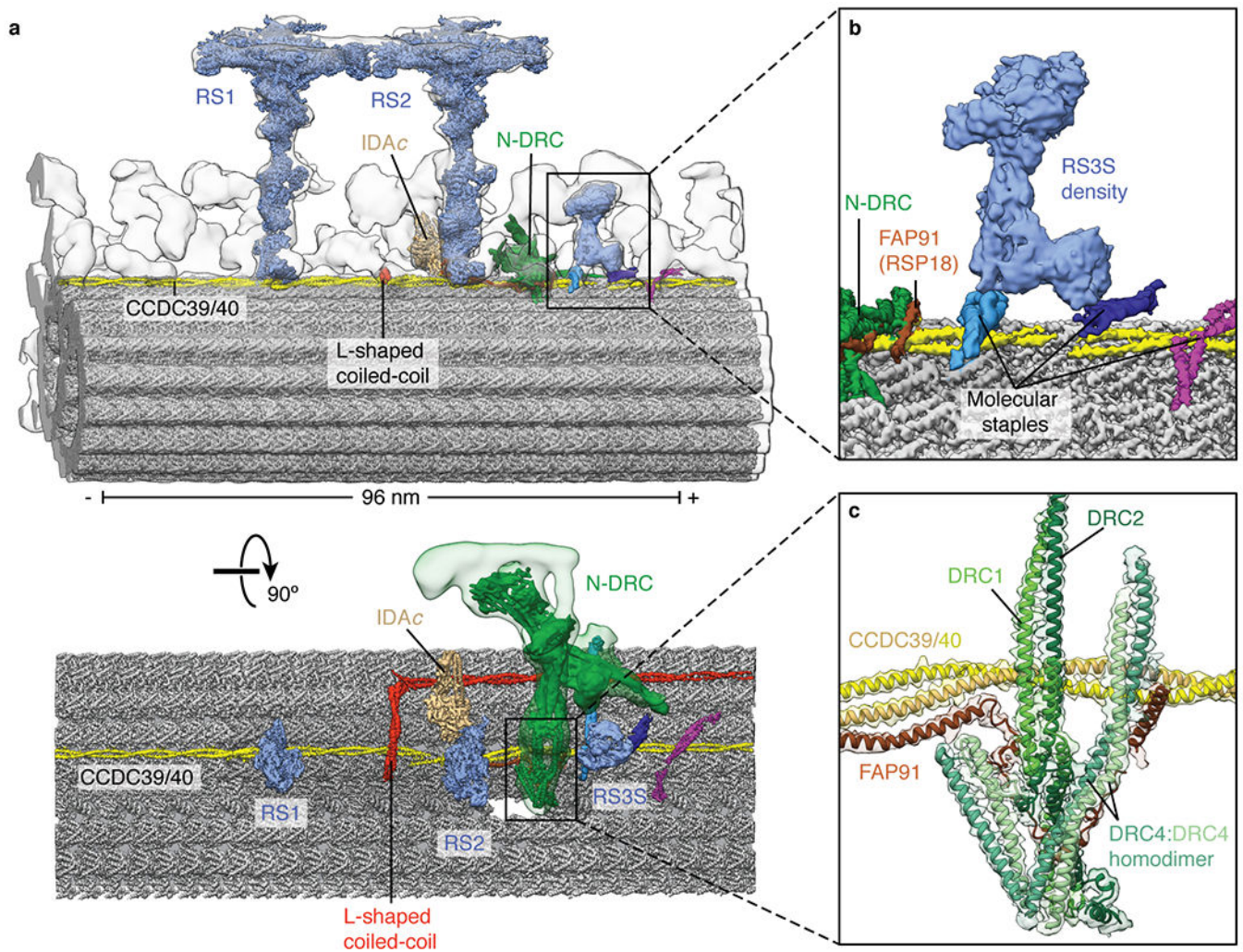
**Extended Data Fig. 4 |. Single-particle cryo-EM maps docked into a subtomogram average of the axoneme.**

a, Two views showing the single-particle cryo-EM maps of RS1, RS2, RS3S, N-DRC, and IDA*c* docked into the subtomogram average of the 96-nm repeat of the *Chlamydomonas* axoneme (EMD-6872). The subtomogram average is shown as a gray isosurface. **b,** Zoom-in view showing the map of RS3S. Density for RS3S is recovered in 25% of the particles following 3D classification (Extended Data Fig. 1b). RS3S interacts with two molecular staples of unknown identity. **c,** Zoom-in view showing the model and map for the N-DRC baseplate. Three N-DRC subunits (DRC1, DRC2, and DRC4) can be unambiguously identified. FAP91 interacts with all three.
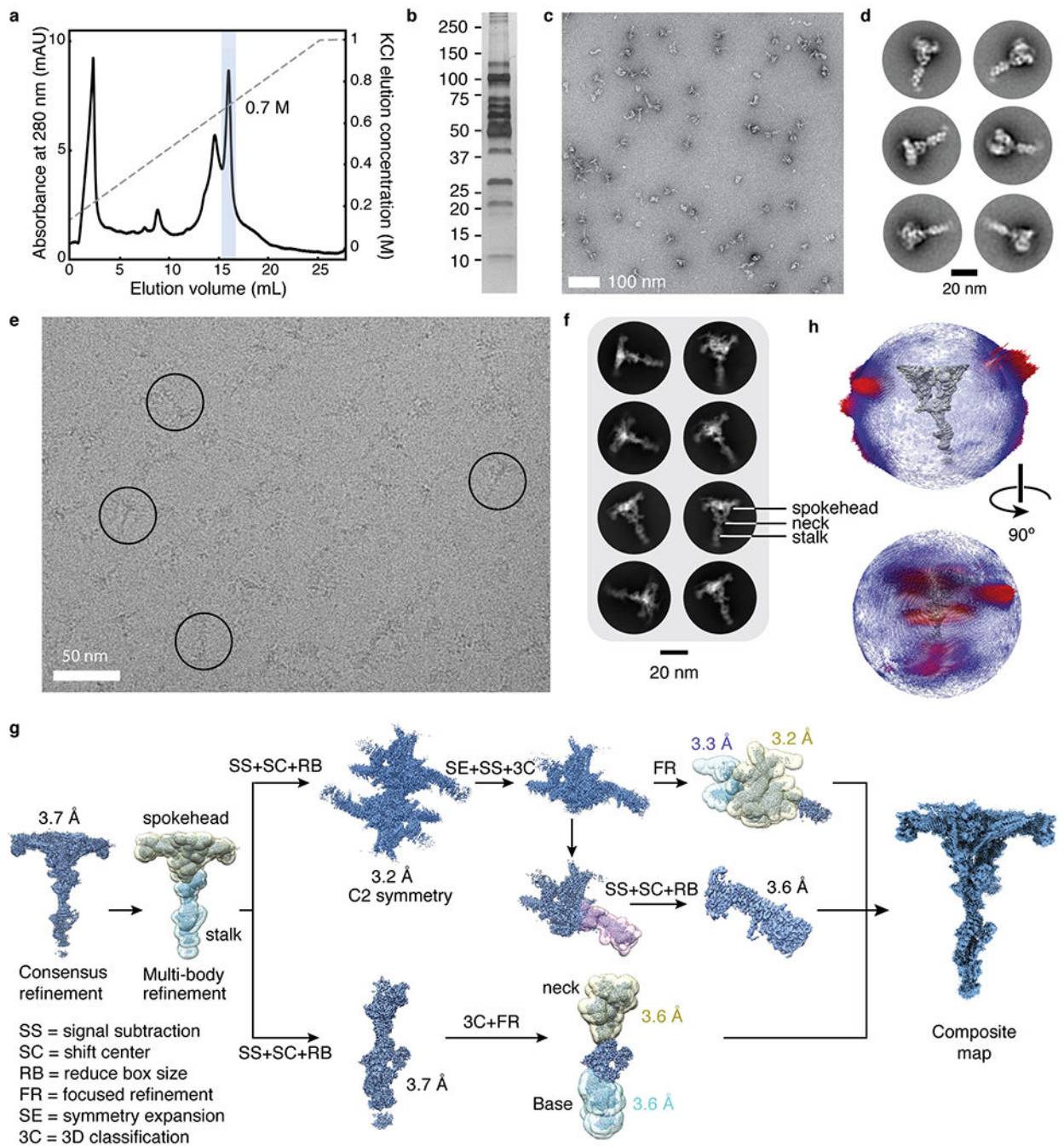
Extended Data Fig. 5 |. Data collection and processing for isolated RS1.

a, Chromatogram showing the elution of RS1 from an anion-exchange column using a KCl gradient. The peak fraction containing RS1 is highlighted and elutes at ~0.7 M KCl. **b**, Silver-stained SDS-PAGE gel showing the purity of isolated RS1 following anion-exchange chromatography. The molecular weights of markers (in kDa) are indicated on the left. The result of mass spectrometry analysis of this sample is given in Supplementary Data 1. **c**, Section of a negative-stain electron micrograph showing homogeneous and monodisperse radial spokes. **d**, Selected two-dimensional class averages of particles selected from

negative-stain electron micrographs. **e,** Section of an electron micrograph showing radial spokes in vitreous ice. Particles showing the characteristic T-shaped projection of radial spokes are circled. **f,** Selected two-dimensional class averages of radial spokes showing well defined spokeheads but nebulous density for the stalk consistent with flexibility at the neck. **g,** Schematic showing the processing of the isolated RS1 data. Following a consensus refinement, the spokehead and stalk were independently refined. The twofold rotational symmetry of the spokehead was exploited to improve the map quality. Further masked refinement was used to improve the flexible projections of the spokehead and the base and neck of the stalk. These individual maps were recombined to generate a final composite cryo-EM map. **h,** Angular distribution of the particle views used for the consensus reconstruction of isolated RS1. The height of the cylinders, colored from blue to red, represents the number of particles. The final density map of RS1 is shown in gray.
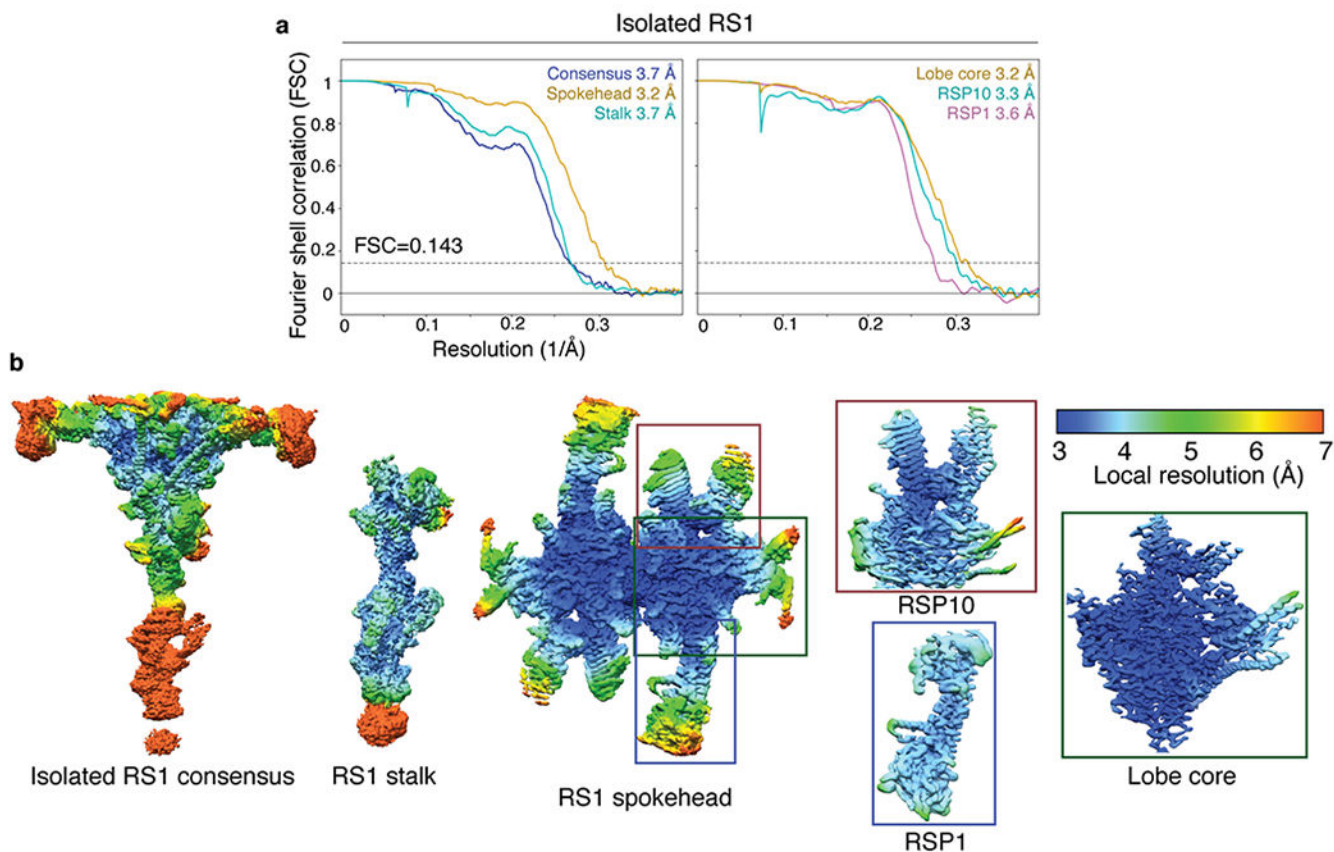
Extended Data Fig. 6 |. Global and local resolution of isolated RS1.
a, FSC curves calculated between masked independent half maps for isolated RS1. Left panel, FSC curves are shown for the consensus refinement of isolated RS1, focused refinement of the stalk, and focused refinement of the spokehead after applying C2 symmetry. Right panel, FSC curves for focused refinements of three subdomains of a single lobe of the RS1 spokehead. The colors of the curves match the masks used in Extended Data Fig. 5g. The nominal resolution was estimated using the FSC = 0.143 criterion (dashed line).

b, Density maps for the consensus refinement of isolated RS1 and various focused refinements colored by local resolution. The local resolution is colored from 3 to 7 Å.
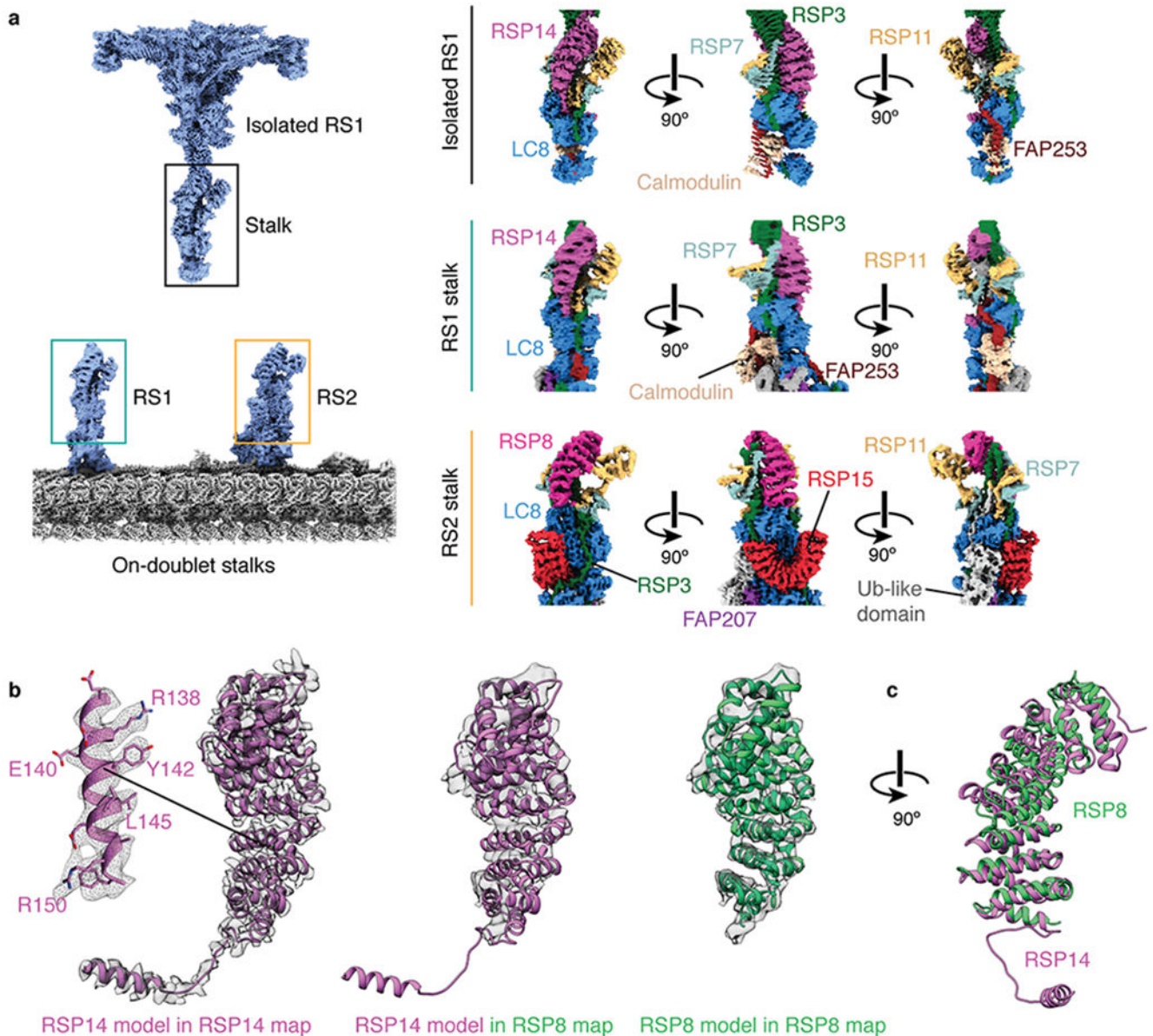
**Extended Data Fig. 7 |. The stalks of RS1 and RS2.**
a, The stalk of the isolated radial spoke is consistent with the on-doublet stalk of RS1 only. FAP253, RSP14, and calmodulin are present in the stalk of RS1 but not RS2. RSP8, RSP15, and an unidentified ubiquitin (Ub)-like domain are present in the stalk of RS2 but not RS1. LC8, FAP207, and RSP3 are common to both RS1 and RS2 but adopt different conformations. The RSP7/11 heterodimer is similar in both radial spokes. **b**, RSP14 and RSP8 are structurally similar armadillo proteins present in different radial spokes. Left, RSP14 was identified in the stalk of RS1 based on well-defined sidechain density. Middle, the model of RSP14 is incompatible with the density of the armadillo protein in RS2,

indicating that they are different proteins with similar folds. Right, a model for RSP8 built into the RS2 density. **c**, Superposition of the atomic models for RSP8 and RSP14.
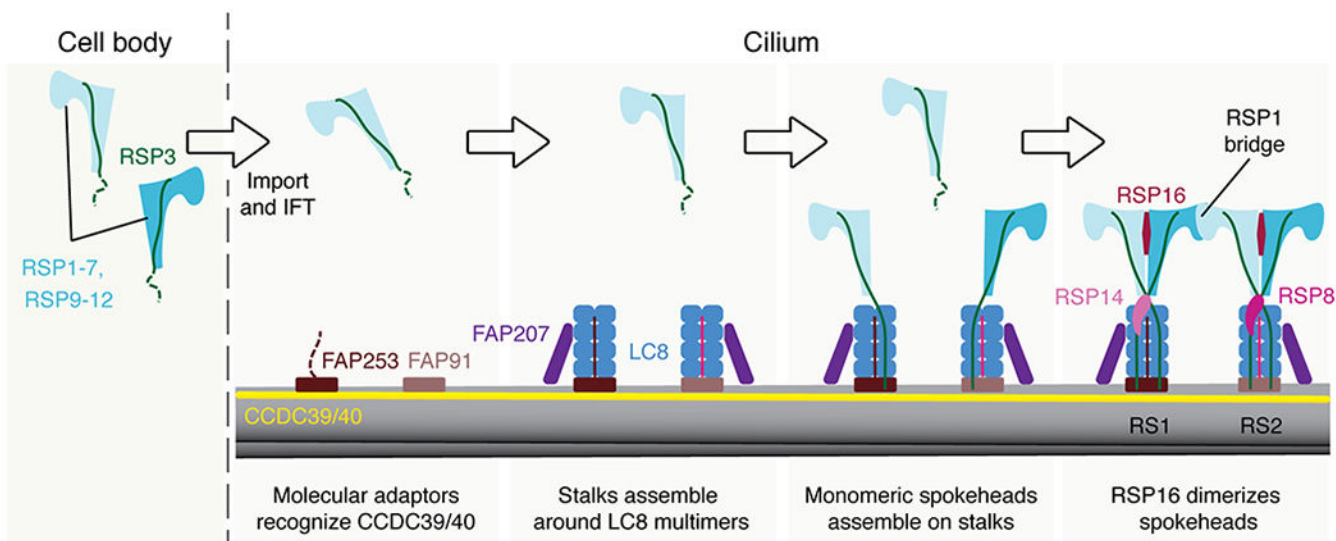

Extended Data Fig. 8 |. Model of radial spoke assembly.
Proposed model of radial spoke assembly. Monomeric spokehead lobes, comprising RSP1-7 and RSP9-12, assemble in the cell body[28,34–36] before being imported into the cilium by intraflagellar transport (IFT)[34,75]. In the cilium, the axonemal doublet microtubules are bound by the CCDC39/40 coiled coil. Specific sequences within the coiled coil are recognized by molecular adaptors FAP253 and FAP91 that establish the binding sites for RS1 and RS2. These molecular adaptors recruit LC8 and FAP207, although the arrangement of these elements is different in the two stalks. RSP3 in the precursor binds the LC8 multimers (Fig. 4b), helping dock the spokehead lobe onto the preassembled stalks. Two lobes can bind a single stalk. Binding of RSP16 is presumably a relatively late step that dimerizes the lobes[28]. At a similar time, RS-specific proteins bind; RSP14 to RS1 and RSP8 to RS2.
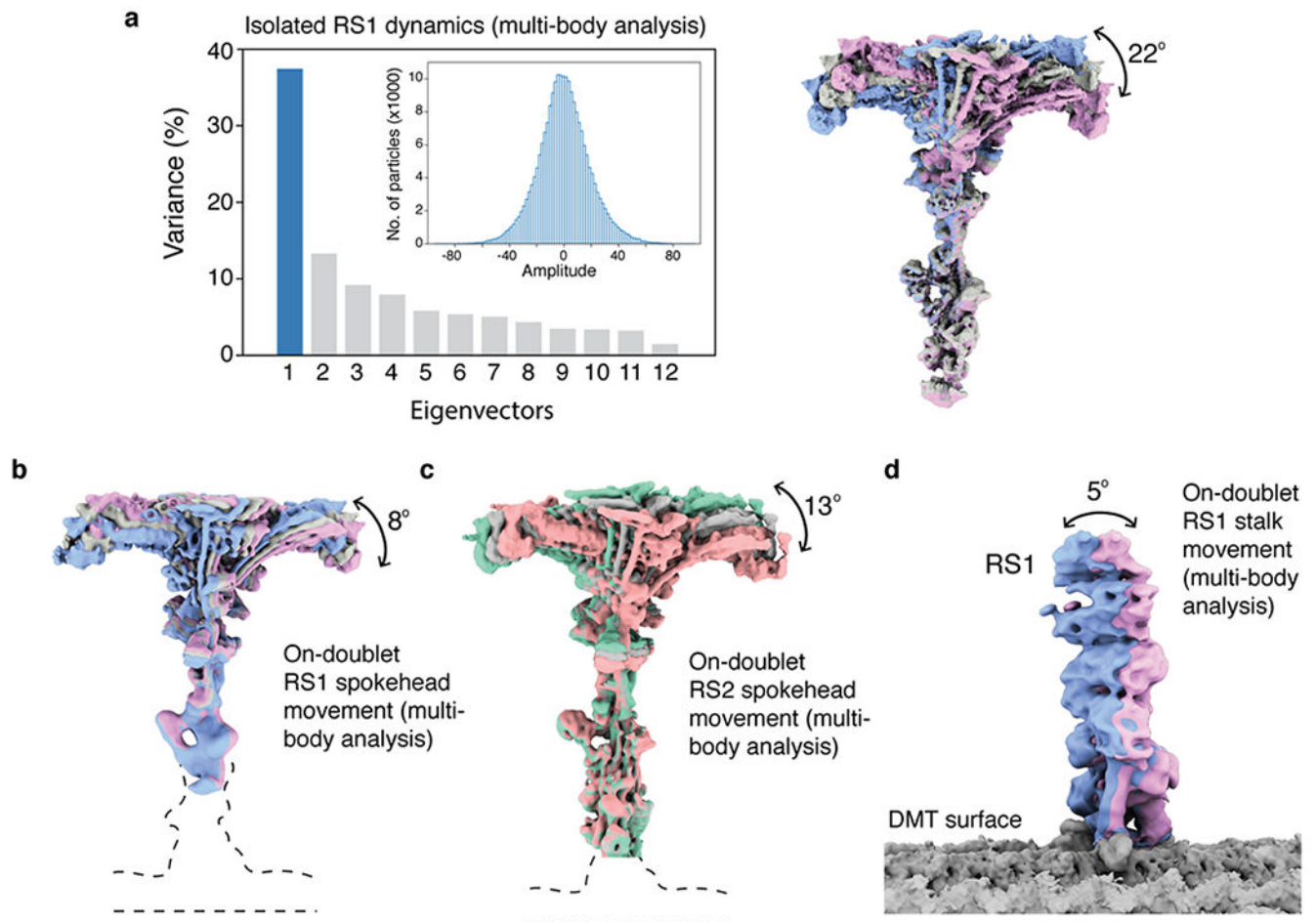
Extended Data Fig. 9 |. Dynamics of radial spokes by multi-body analysis.
a, Multi-body analysis of isolated RS1. Left, the contributions of all eigenvectors to the variance. The first eigenvector accounts for 37% of all variability. Inset, the unimodal histogram of amplitudes along the first eigenvector indicates continuous motion. Right, the density maps at the extremes and middle show the same tilting of the spokehead relative to the stalk as observed by the neural-network approach in Fig. 6a. **b**, Multi-body analysis of on-doublet RS1 shows the same direction of spokehead tilt as isolated RS1. **c**, Multi-body analysis of on-doublet RS2 shows that the spokeheads of both radial spokes tilt in similar directions to similar extents. **d**, Multi-body analysis of the movement of the RS1 stalk with respect to the doublet microtubule (DMT) surface.
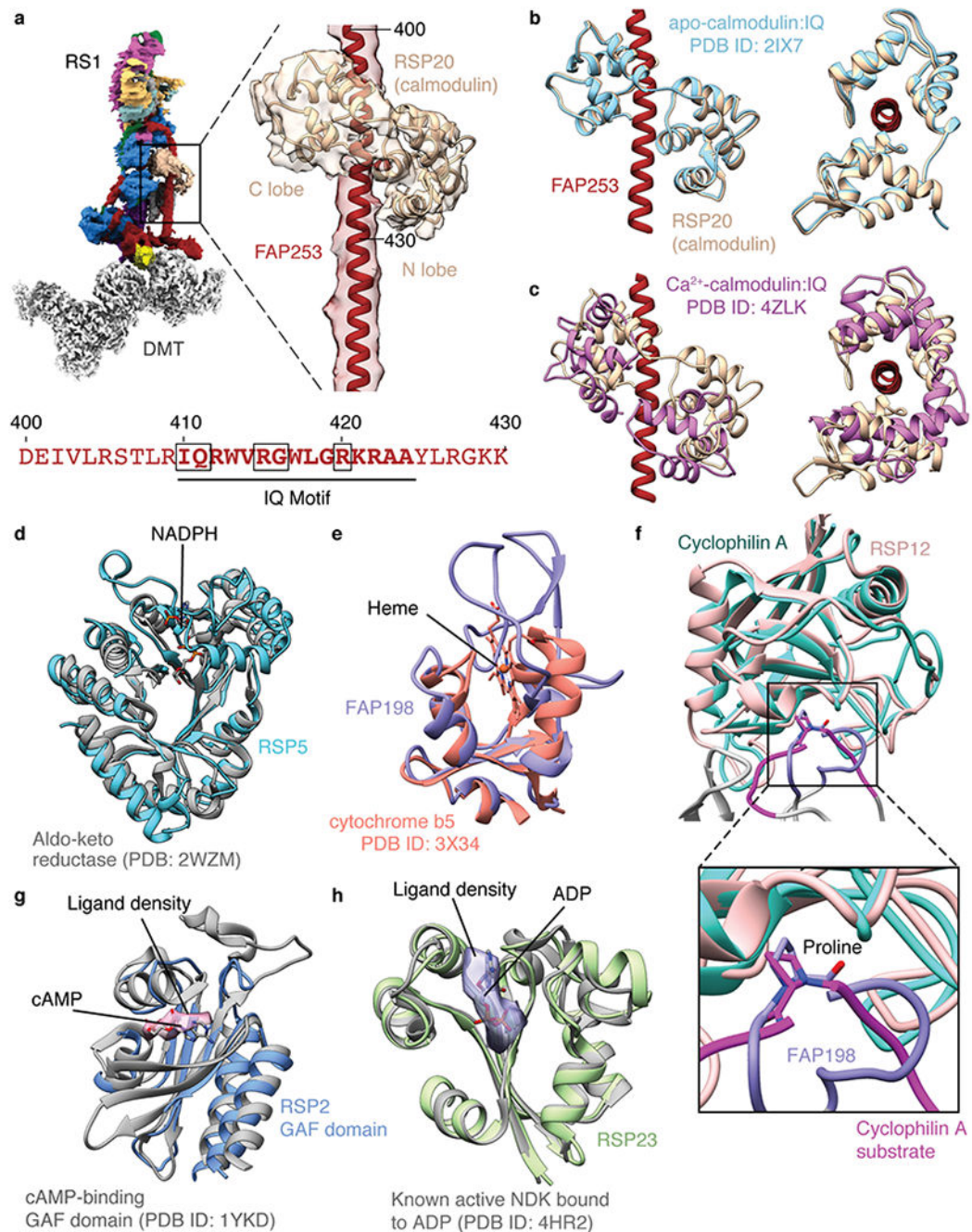
Extended Data Fig. 10 |. Potential chemical modulation of radial spokes.
a, Calmodulin binds the IQ motif of FAP253 at the base of RS1. Below, sequence of FAP253 residues 400-430 showing the presence of an IQ motif (emboldened with motif-defining residues boxed). **b**, Structural comparison of calmodulin bound to FAP253 with apo-calmodulin bound to an IQ motif from myosin V (PDB 2IX7)[42]. **c**, Structural comparison of calmodulin bound to FAP253 with Ca^{2+}-calmodulin bound to an IQ motif from myosin 5a (PDB 4ZLK)[42]. **d**, The structure of RSP5 resembles an NADPH-dependent aldo-keto reductase domain (PDB 2WZM)[76]. However, the NADPH binding site of RSP5 is

absent and filled by two loops (residues 393-414 and 468-484 of RSP5). **e**, The N-terminal domain of FAP198 closely resembles heme-binding cytochrome b5 (PDB 3X34)[77]. However, no heme is observed bound to FAP198, and the putative heme-binding site is occluded by a loop of FAP198 (residues 89-95). **f**, RSP12 structurally resembles cylophilin-type peptidyl-prolyl *cis-trans* isomerase (PDB 1AK4)[78]. The putative substrate-binding site of RSP12 is occupied by a loop of FAP198 (residues 96-105), which positions a proline (P99) in the active site. **g**, Atomic model of the GAF domain from RSP2 superposed with the model of a cAMP-bound GAF domain (PDB 1YKD)[79]. Unexplained density in the RSP2 GAF domain (pink, contoured at 0.01) is observed in the cAMP binding pocket, but the resolution is insufficient to assign it as a cyclic nucleotide. The cAMP ligand from PDB 1YKD is shown for comparison. **h**, Atomic model of RSP23 superposed with an active, ADP-bound nucleoside diphosphate kinase (NDK; PDB 4HR2). Many of the active site residues are conserved. Potential density for a bound nucleotide to RSP23 is observed in the on-doublet map of RS1 (purple, contoured at 0.017) but not in the isolated RS1 map. The ADP ligand from PDB 4HR2 is shown for comparison.

Supplementary Material

Refer to Web version on PubMed Central for supplementary material.

Acknowledgments

References

1. Ginger ML, Portman N & McKean PG Swimming with protists: perception, motility and flagellum assembly. Nat Rev Micro 6, 838–850 (2008).

2. Bustamante-Marin XM & Ostrowski LE Cilia and Mucociliary Clearance. Cold Spring Harbor Perspectives in Biology 9, a028241 (2017). [PubMed: 27864314]

3. Lyons RA, Saridogan E & Djahanbakhch O The reproductive significance of human Fallopian tube cilia. Hum. Reprod. Update 12, 363–372 (2006). [PubMed: 16565155]

4. Faubel R, Westendorf C, Bodenschatz E & Eichele G Cilia-based flow network in the brain ventricles. Science 353, 176–178 (2016). [PubMed: 27387952]

5. Nonaka S et al. Randomization of left-right asymmetry due to loss of nodal cilia generating leftward flow of extraembryonic fluid in mice lacking KIF3B motor protein. Cell 95, 829–837 (1998). [PubMed: 9865700]

6. Ishikawa T Axoneme Structure from Motile Cilia. Cold Spring Harbor Perspectives in Biology 9, a028076 (2017). [PubMed: 27601632]

7. Brokaw CJ & Kamiya R Bending patterns of Chlamydomonas flagella: IV. Mutants with defects in inner and outer dynein arms indicate differences in dynein arm function. Cell Motil. Cytoskeleton 8, 68–75 (1987). [PubMed: 2958145]

8. Lin J & Nicastro D Asymmetric distribution and spatial switching of dynein activity generates ciliary motility. Science 360, eaar1968 (2018). [PubMed: 29700238]

9. Heuser T, Raytchev M, Krell J, Porter ME & Nicastro D The dynein regulatory complex is the nexin link and a major regulatory node in cilia and flagella. J. Cell Biol 187, 921–933 (2009). [PubMed: 20008568]

10. Bower R et al. The N-DRC forms a conserved biochemical complex that maintains outer doublet alignment and limits microtubule sliding in motile axonemes. Mol. Biol. Cell 24, 1134–1152 (2013). [PubMed: 23427265]

11. Luck D, Piperno G, Ramanis Z & Huang B Flagellar mutants of Chlamydomonas: studies of radial spoke-defective strains by dikaryon and revertant analysis. Proc. Natl. Acad. Sci. U.S.A 74, 3456–3460 (1977). [PubMed: 269405]

12. Smith EF & Sale WS Regulation of dynein-driven microtubule sliding by the radial spokes in flagella. Science 257, 1557–1559 (1992). [PubMed: 1387971]

13. Pigino G et al. Cryoelectron tomography of radial spokes in cilia and flagella. J. Cell Biol 195, 673–687 (2011). [PubMed: 22065640]

14. Barber CF, Heuser T, Carbajal González BI, Botchkarev VV & Nicastro D Three-dimensional structure of the radial spokes reveals heterogeneity and interactions with dyneins in Chlamydomonas flagella. Mol. Biol. Cell 23, 111–120 (2012). [PubMed: 22072792]

15. Lin J et al. Cryo-electron tomography reveals ciliary defects underlying human RSPH1 primary ciliary dyskinesia. Nat Commun 5, 5727 (2014). [PubMed: 25473808]

16. Lin J et al. Building blocks of the nexin-dynein regulatory complex in Chlamydomonas flagella. J. Biol. Chem 286, 29175–29191 (2011). [PubMed: 21700706]

17. Piperno G, Huang B & Luck DJ Two-dimensional analysis of flagellar proteins from wild-type and paralyzed mutants of Chlamydomonas reinhardtii. Proc. Natl. Acad. Sci. U.S.A 74, 1600–1604 (1977). [PubMed: 266200]

18. Piperno G, Huang B, Ramanis Z & Luck DJ Radial spokes of Chlamydomonas flagella: polypeptide composition and phosphorylation of stalk components. J. Cell Biol 88, 73–79 (1981). [PubMed: 6451632]

19. Yang P, Diener DR, Rosenbaum JL & Sale WS Localization of calmodulin and dynein light chain LC8 in flagellar radial spokes. J. Cell Biol 153, 1315–1326 (2001). [PubMed: 11402073]

20. Reiter JF & Leroux MR Genes and molecular pathways underpinning ciliopathies. Nat. Rev. Mol. Cell Biol 18, 533–547 (2017). [PubMed: 28698599]

21. Ma M et al. Structure of the Decorated Ciliary Doublet Microtubule. Cell 179, 909–922.e12 (2019). [PubMed: 31668805]

22. Oda T, Yanagisawa H, Kamiya R & Kikkawa M Cilia and flagella. A molecular ruler determines the repeat length in eukaryotic cilia and flagella. Science 346, 857–860 (2014). [PubMed: 25395538]

23. Lin H et al. A NIMA-Related Kinase Suppresses the Flagellar Instability Associated with the Loss of Multiple Axonemal Structures. PLoS Genet. 11, e1005508 (2015). [PubMed: 26348919]

24. Dymek EE, Heuser T, Nicastro D & Smith EF The CSC is required for complete radial spoke assembly and wild-type ciliary motility. Mol. Biol. Cell 22, 2520–2531 (2011). [PubMed: 21613541]

25. Urbanska P et al. The CSC proteins FAP61 and FAP251 build the basal substructures of radial spoke 3 in cilia. Mol. Biol. Cell 26, 1463–1475 (2015). [PubMed: 25694453]

26. Oda T, Yagi T, Yanagisawa H & Kikkawa M Identification of the outer-inner dynein linker as a hub controller for axonemal dynein activities. Curr. Biol 23, 656–664 (2013). [PubMed: 23583547]

27. Poghosyan E et al. The structure and symmetry of radial spoke protein complex in Chlamydomonas flagella. J. Cell. Sci jcs.245233 (2020).

28. Yang C, Compton MM & Yang P Dimeric novel HSP40 is incorporated into the radial spoke complex during the assembly process in flagella. Mol. Biol. Cell 16, 637–648 (2005). [PubMed: 15563613]

29. Zhu X et al. The roles of a flagellar HSP40 ensuring rhythmic beating. Mol. Biol. Cell 30, 228–241 (2019). [PubMed: 30427757]

30. El Khouri E, et al. Mutations in DNAJB13, Encoding an HSP40 Family Member, Cause Primary Ciliary Dyskinesia and Male Infertility. Am. J. Hum. Genet 99, 489–500 (2016). [PubMed: 27486783]

31. Warner FD & Satir P The structural basis of ciliary bend formation. Radial spoke positional changes accompanying microtubule sliding. J. Cell Biol 63, 35–63 (1974). [PubMed: 4424314]

32. Goodenough UW, Adair WS, Collin-Osdoby P & Heuser JE Structure of the Chlamydomonas agglutinin and related flagellar surface proteins in vitro and in situ. J. Cell Biol 101, 924–941 (1985). [PubMed: 4030899]

33. Kubo T, Hou Y, Cochran DA, Witman GB & Oda T A microtubule-dynein tethering complex regulates the axonemal inner dynein f (I1). Mol. Biol. Cell 29, 1060–1074 (2018). [PubMed: 29540525]

34. Qin H, Diener DR, Geimer S, Cole DG & Rosenbaum JL Intraflagellar transport (IFT) cargo IFT transports flagellar precursors to the tip and turnover products to the cell body. J. Cell Biol 164, 255–266 (2004). [PubMed: 14718520]

35. Diener DR et al. Sequential assembly of flagellar radial spokes. Cytoskeleton (Hoboken) 68, 389–400 (2011). [PubMed: 21692193]

36. Gupta A, Diener DR, Sivadas P, Rosenbaum JL & Yang P The versatile molecular complex component LC8 promotes several distinct steps of flagellar assembly. J. Cell Biol 198, 115–126 (2012). [PubMed: 22753897]

37. Oda T, Yanagisawa H, Yagi T & Kikkawa M Mechanosignaling between central apparatus and radial spokes controls axonemal dynein activity. J. Cell Biol 204, 807–819 (2014). [PubMed: 24590175]

38. Gaillard AR, Diener DR, Rosenbaum JL & Sale WS Flagellar radial spoke protein 3 is an A-kinase anchoring protein (AKAP). J. Cell Biol 153, 443–448 (2001). [PubMed: 11309423]

39. LeDizet M & Piperno G The light chain p28 associates with a subset of inner dynein arm heavy chains in Chlamydomonas axonemes. Mol. Biol. Cell 6, 697–711 (1995). [PubMed: 7579689]

40. Kagami O & Kamiya R Translocation and rotation of microtubules caused by multiple species of Chlamydomonas inner-arm dynein. J. Cell. Sci 103, 653–664 (1992).

41. Yanagisawa H-A & Kamiya R Association between Actin and Light Chains in Chlamydomonas Flagellar Inner-Arm Dyneins. Biochemical and Biophysical Research Communications 288, 443–447 (2001). [PubMed: 11606062]

42. Houdusse A et al. Crystal structure of apo-calmodulin bound to the first two IQ motifs of myosin V reveals essential recognition features. Proc. Natl. Acad. Sci. U.S.A 103, 19326–19331 (2006). [PubMed: 17151196]

43. Shen M et al. Calmodulin in complex with the first IQ motif of myosin-5a functions as an intact calcium sensor. Proc. Natl. Acad. Sci. U.S.A 113, E5812–E5820 (2016). [PubMed: 27647889]

44. Bessen M, Fay RB & Witman GB Calcium control of waveform in isolated flagellar axonemes of Chlamydomonas. J. Cell Biol 86, 446–455 (1980). [PubMed: 6447155]

45. King SM & Patel-King RS Identification of a Ca(2+)-binding light chain within Chlamydomonas outer arm dynein. J. Cell. Sci 108 (Pt 12), 3757–3764 (1995). [PubMed: 8719882]

46. Price ME & Sisson JH Redox regulation of motile cilia in airway disease. Redox Biol 27, 101146 (2019). [PubMed: 30833143]

47. Lindemann CB A cAMP-induced increase in the motility of demembranated bull sperm models. Cell 13, 9–18 (1978). [PubMed: 202401]

48. Smith EF & Yang P The radial spokes and central apparatus: mechano-chemical transducers that regulate flagellar motility. Cell Motil. Cytoskeleton 57, 8–17 (2004). [PubMed: 14648553]

49. Yang P et al. Radial spoke proteins of Chlamydomonas flagella. J. Cell. Sci 119, 1165–1174 (2006). [PubMed: 16507594]

50. Lindemann CB & Lesich KA The geometric clutch at 20: stripping gears or gaining traction? Reproduction 150, R45–53 (2015). [PubMed: 25918437]

51. Yagi T et al. An axonemal dynein particularly important for flagellar movement at high viscosity. Implications from a new Chlamydomonas mutant deficient in the dynein heavy chain gene DHC9. J. Biol. Chem 280, 41412–41420 (2005). [PubMed: 16236707]

52. Kamiya R Extrusion and Rotation of the central-pair microtubules in detergent-treated Chlamydomonas flagella. Prog. Clin. Biol. Res 80, 169–173 (1982). [PubMed: 7100176]

53. Omoto CK et al. Rotation of the central pair microtubules in eukaryotic flagella. Mol. Biol. Cell 10, 1–4 (1999). [PubMed: 9880321]

54. Mitchell DR Orientation of the central pair complex during flagellar bend formation in Chlamydomonas. Cell Motil. Cytoskeleton 56, 120–129 (2003). [PubMed: 14506709]

55. Satouh Y & Inaba K Proteomic characterization of sperm radial spokes identifies a novel spoke protein with an ubiquitin domain. FEBS Letters 583, 2201–2207 (2009). [PubMed: 19527718]

56. Sager R & Granick S Nutritional control of sexuality in Chlamydomonas reinhardi. J. Gen. Physiol 37, 729–742 (1954). [PubMed: 13174779]

57. Craige B, Brown JM & Witman GB Isolation of Chlamydomonas flagella. Curr Protoc Cell Biol Chapter 3, Unit 3.41.1–9 (2013).

58. Zivanov J et al. New tools for automated high-resolution cryo-EM structure determination in RELION-3. elife 7, 163 (2018).

59. Schorb M, Haberbosch I, Hagen WJH, Schwab Y & Mastronarde DN Software tools for automated transmission electron microscopy. Nat. Methods 16, 471–477 (2019). [PubMed: 31086343]

60. Pettersen EF et al. UCSF Chimera--a visualization system for exploratory research and analysis. J Comput Chem 25, 1605–1612 (2004). [PubMed: 15264254]

61. Zheng SQ et al. MotionCor2: anisotropic correction of beam-induced motion for improved cryo-electron microscopy. Nat. Methods 14, 331–332 (2017). [PubMed: 28250466]

62. Rohou A & Grigorieff N CTFFIND4: Fast and accurate defocus estimation from electron micrographs. J Struct Biol 192, 216–221 (2015). [PubMed: 26278980]

63. Wagner T et al. SPHIRE-crYOLO is a fast and accurate fully automated particle picker for cryo-EM. Commun Biol 2, 218–13 (2019). [PubMed: 31240256]

64. Zhang K et al. Cryo-EM Reveals How Human Cytoplasmic Dynein Is Auto-inhibited and Activated. Cell 169, 1303–1314.e18 (2017). [PubMed: 28602352]

65. Nakane T, Kimanius D, Lindahl E & Scheres SH Characterisation of molecular motions in cryo-EM single-particle data by multi-body refinement in RELION. elife 7, 1485 (2018).

66. Scheres SHW Processing of Structurally Heterogeneous Cryo-EM Data in RELION. Meth. Enzymol 579, 125–157 (2016).

67. Zhong ED, Bepler T, International JD2020. Reconstructing continuous distributions of 3D protein structure from cryo-EM images. bioRxiv

68. Emsley P, Lohkamp B, Scott WG & Cowtan K Features and development of Coot. Acta Crystallogr. D Biol. Crystallogr 66, 486–501 (2010). [PubMed: 20383002]

69. Pazour GJ, Agrin N, Leszyk J & Witman GB Proteomic analysis of a eukaryotic cilium. J. Cell Biol 170, 103–113 (2005). [PubMed: 15998802]

70. Afonine PV et al. Real-space refinement in PHENIX for cryo-EM and crystallography. Acta Crystallogr D Struct Biol 74, 531–544 (2018). [PubMed: 29872004]

71. Chen VB et al. MolProbity: all-atom structure validation for macromolecular crystallography. Acta Crystallogr. D Biol. Crystallogr 66, 12–21 (2010). [PubMed: 20057044]

72. Goddard TD et al. UCSF ChimeraX: Meeting modern challenges in visualization and analysis. Protein Sci. 27, 14–25 (2018). [PubMed: 28710774]

73. Schrödinger LLC. The PyMOL Molecular Graphics System, Version 2.0

74. Morin A et al. Collaboration gets the most out of software. elife 2, e01456 (2013). [PubMed: 24040512]

75. Lechtreck KF, Mengoni I, Okivie B & Hilderhoff KB In vivo analyses of radial spoke transport, assembly, repair and maintenance. Cytoskeleton (Hoboken) 75, 352–362 (2018). [PubMed: 30070024]

76. Scoble J et al. Crystal structure and comparative functional analyses of a Mycobacterium aldo-keto reductase. Journal of Molecular Biology 398, 26–39 (2010). [PubMed: 20188740]

77. Hirano Y, Kimura S & Tamada T High-resolution crystal structures of the solubilized domain of porcine cytochrome b5. Acta Crystallogr. D Biol. Crystallogr 71, 1572–1581 (2015). [PubMed: 26143928]

78. Gamble TR et al. Crystal structure of human cyclophilin A bound to the amino-terminal domain of HIV-1 capsid. Cell 87, 1285–1294 (1996). [PubMed: 8980234]

79. Martinez SE et al. Crystal structure of the tandem GAF domains from a cyanobacterial adenylyl cyclase: modes of ligand binding and dimerization. Proc. Natl. Acad. Sci. U.S.A 102, 3082–3087 (2005). [PubMed: 15708973]
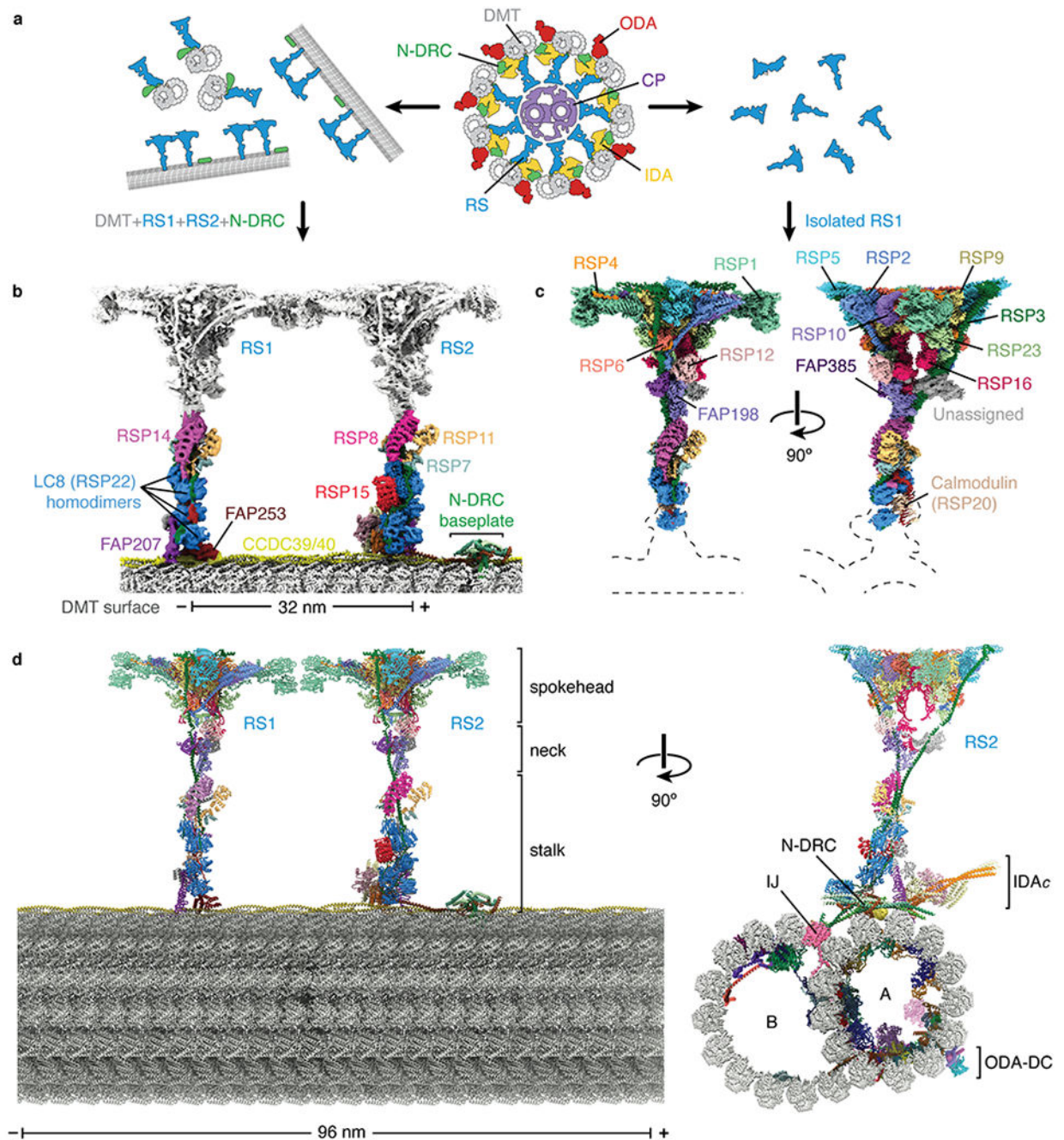
Fig. 1 |. Structures of radial spokes on and off doublet microtubules.
a, Schematic representation showing biochemical fragmentation of the *Chlamydomonas* axoneme (viewed in cross-section; center) into mechanoregulator-bound doublet microtubules (left) and isolated radial spokes (right). The axoneme consists of a central pair of microtubules (CP, purple) surrounded by doublet microtubules (DMT; gray) bound by radial spokes (RS; blue), nexin-dynein regulatory complexes (N-DRC; green), inner dynein arm (IDA; yellow), and outer dynein arm (ODA; red). **b**, Composite density map for on-doublet RS1 and RS2. The maps of the stalks are colored by subunit. The neck and

spokehead, which are less well resolved, are colored gray. **c**, Orthogonal views of a composite density map for isolated RS1 with the map colored by subunit. Dashed lines indicate the positions of the stalks and doublet microtubule which are not present in the reconstruction. **d**, Orthogonal views of an atomic model for the 96-nm repeat of the doublet microtubule. The model combines atomic models of the doublet-bound stalks of RS1 and RS2, and the stalk, neck, and spokehead of isolated RS1 with model of the doublet microtubule (PDB 6U42)[21]. Individual subunits are colored according to panels b and c. In panels b and d, the minus (−) and plus (+) ends of the doublet microtubule are indicated at the ends of the scale bar.
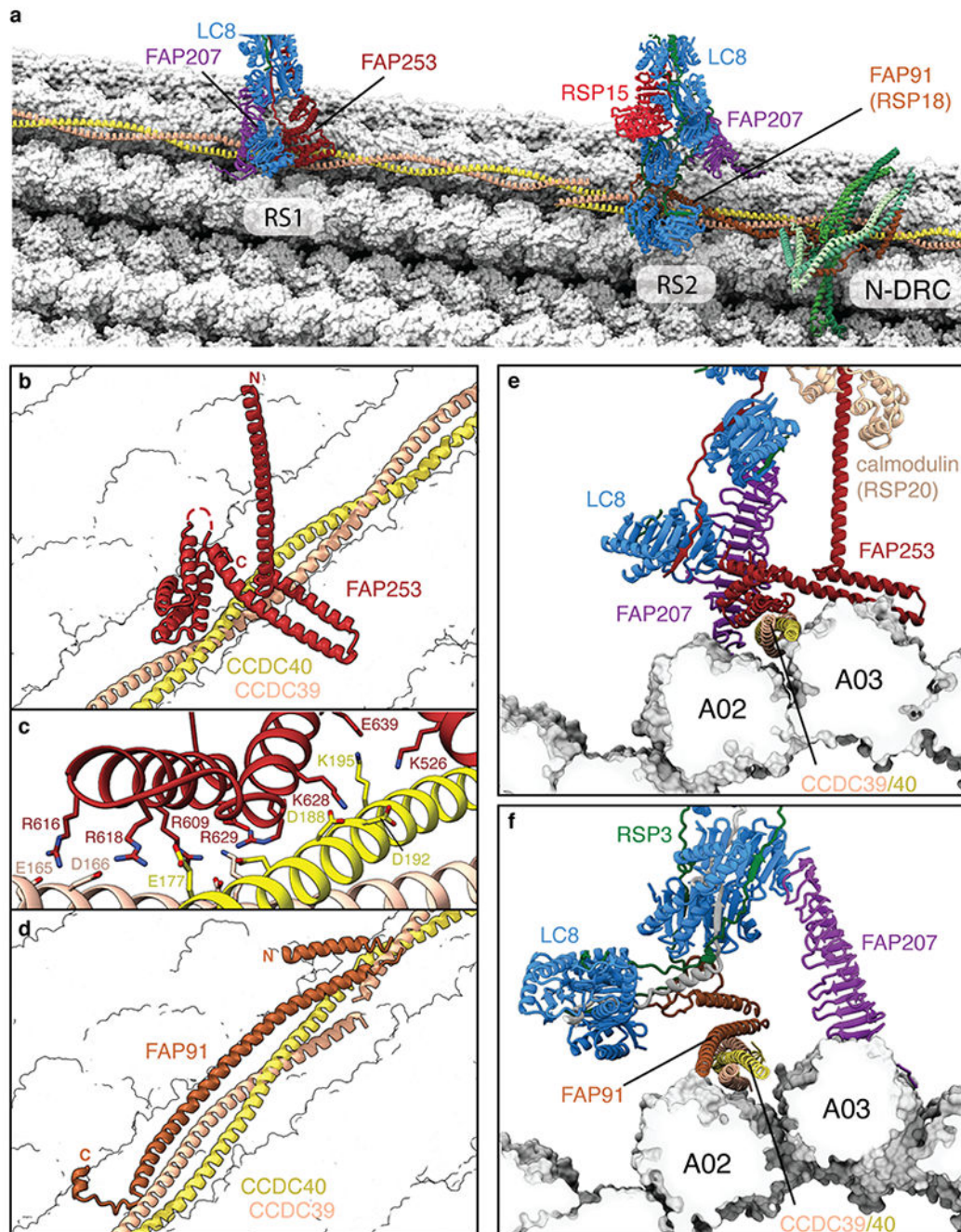
Fig. 2 |. Structural basis for the microtubule docking and longitudinal periodicity of radial spokes.

a, Overview showing the bases of radial spokes 1 and 2 (RS1 and RS2) bound to the doublet microtubule. The radial spoke subunits (LC8, FAP91, FAP207, FAP253, and RSP15), the CCDC39/40 molecular ruler, and the subunits of the nexin-dynein regulatory complex (N-DRC) baseplate are shown as cartoons. Tubulin is shown in surface representation. **b**, The binding site for RS1 is determined by recognition of CCDC39/40 by FAP253. **c**, Zoom-in view showing that the interface between FAP253 and CCDC39/40 is dominated by a

network of salt bridges. **d**, The binding site for RS2 is determined by FAP91 (RSP18) which forms a triple coiled coil with CCDC39/40. **e**, Cross-section view of the RS1-doublet microtubule interaction showing recognition of CCDC39/40 by FAP253. FAP207 bridges LC8 with protofilament A02. **f**, Cross-section view of the RS2-doublet microtubule interaction showing recognition of CCDC39/40 by FAP91. FAP207 bridges LC8 with protofilament A03.
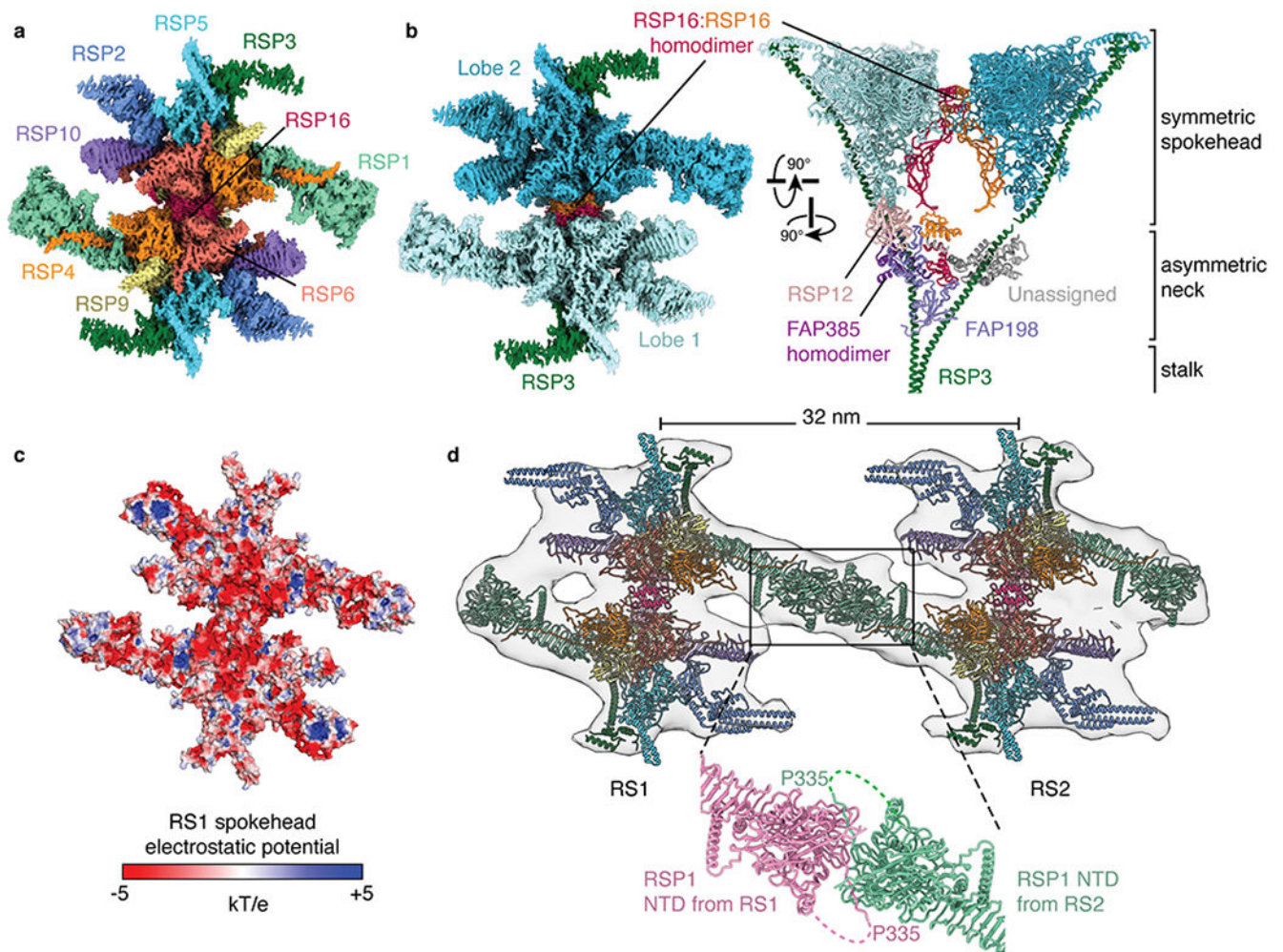
Fig. 3 |. Structure of the radial spokehead.
a, View of the top of the radial spokehead. Composite map colored by subunit. **b,** Two views of the radial spokehead. The two symmetric lobes of the spokehead (colored different shades of blue) are dimerized by a homodimer of RSP16 and flanked by the α-helices of RSP3. The symmetric spokehead sits on a V-shaped asymmetric neck containing FAP198, FAP385, RSP12, and the N-terminal domains of RSP16. **c,** Atomic model of the radial spokehead colored by electrostatic potential. **d,** Atomic models of the radial spokes docked into an isosurface rendering of the subtomogram average of the *Chlamydomonas* axoneme (EMD-6872). The two radial spokes interact through the N-terminal domains (NTD) of RSP1. The zoom-in shows the model of the on-doublet interaction between the NTDs of RSP1 from RS1 and RS2.

Fig. 4 |. Interactions between RSP3 and radial spoke proteins.
a, Left, atomic model of RS1 with its two molecules of RSP3 colored green. Colored boxes indicate the binding sites on RSP3 of five different dimers. The partially boxed proximal region of the stalk is shown in detail in panel b. Right, atomic models of the interactions between RSP3 and different dimers. The sequence alignment shows amphipathic helices of RSP3 with hydrophobic residues recognized by the various dimers colored red. The four-helix bundle of RSP7/RSP11 belongs to the RIIa dimerization/docking domain and the four-helix bundles of RSP4/RSP6, RSP2/RSP23, RSP385/RSP385 and the unassigned dimer belong to Dpy-30 domain (which has an additional helix at the N-terminus compared with RIIa dimerization/docking domain). **b**, Left, orthogonal views of the interactions of RSP3 and FAP253 with the LC8 homodimers in RS1. Other subunits have been omitted for clarity. Right, a schematic showing the resolved LC8-binding motifs of FAP253 and RSP3. **c**, Orthogonal views of the interactions between RSP3 and the LC8 homodimers in RS2. An unassigned protein (pink) also interacts with the β-edges of LC8. Other subunits have been omitted for clarity.

Fig. 5 |. IDA subforms *a* and *c* dock onto the bases of radial spokes.
a, Left, composite map showing the densities for the base of radial spoke 2 (RS2), inner dynein arm subform *c* (IDA*c*), and the doublet microtubule (DMT). The maps of RS2 and IDA*c* are colored by subunit. Right, atomic model of IDA*c* showing the interaction with FAP207 and an unidentified ubiquitin-like domain of RS2. The unassigned helices of IDA*c* may correspond to the tail of the dynein heavy chain. **b**, Left, slice through the subtomogram average of the *Chlamydomonas* axoneme (EMD-6872) with RS2 colored blue, IDA*c* colored yellow, outer dynein arm (ODA) colored red, and the DMT colored gray. Zoomed-in view showing the models of RS2 and IDA*c* (colored blue and yellow, respectively) docking into the subtomogram average. **c**, Left, slice through the subtomogram average of the *Chlamydomonas* axoneme (EMD-6872) with radial spoke 1 (RS1) colored blue, inner dynein arm subform *a* (IDA*a*) colored yellow, ODA colored red, and the DMT colored gray. Zoomed-in view showing the atomic models of RS1 and IDA*c* (colored blue and yellow, respectively) docking into the subtomogram average. The putative interface between IDA*a* and RS1 is distinct from the interface between RS2 and IDA*c*. **d**, Details of the expected interface between RS1 and IDA*a* based on docking the model of IDA*c* into the subtomogram average map of IDA*a* (EMD-6872).
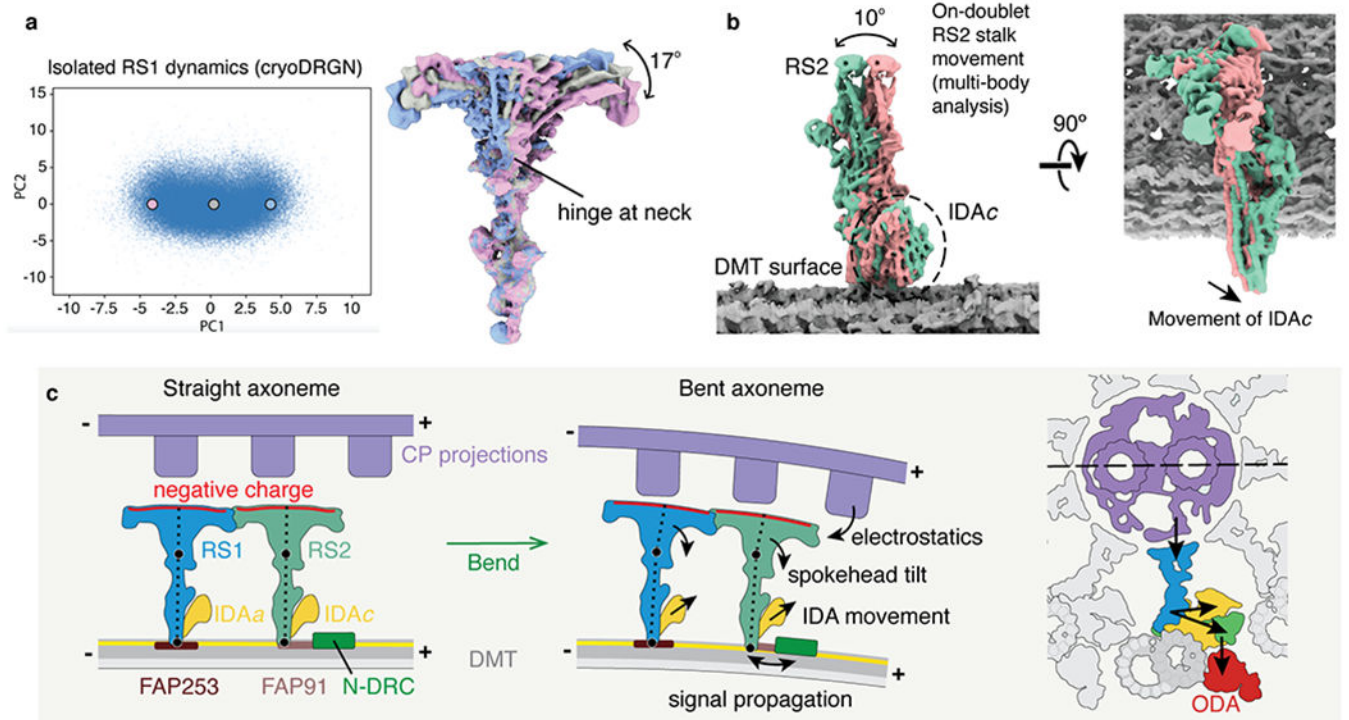
Fig. 6 |. Molecular basis for the control of IDA motor activity by mechanical signals.
a, Conformational dynamics of isolated radial spoke 1 (RS1) inferred from deep neural networks. Left, Principle component (PC) analysis projection of latent space. Density maps were generated at three points along PC1. Right, Density maps generated from these 3 points were aligned on the stalk and show tilting of the spokehead relative to the stalk. The hinge lies in the neck. **b**, Multi-body analysis of the movement of the RS2 stalk and IDA*c* with respect to the doublet microtubule (DMT) surface. The DMT, RS2, and IDA*c* were separately masked and treated as individual bodies free to move relative to one another. Movement of IDA*c* corresponds with the movement of the RS2 stalk. **c**, A model for mechanoregulation of ciliary motility. As the axoneme bends, the projections of the central pair (CP) are brought closer to the spokeheads. An increase in the electrostatic force with decreasing distance causes the radial spoke to tilt at two hinge points (indicated with black circles). As the movement of IDA*c* is coupled to the movement of RS2, tilting of the radial spoke changes the orientation of the IDA. IDA*a* may likewise be coupled to the movement of RS1. Signals may propagate from RS2 to N-DRC through FAP91 and the CCDC39/40 coiled coil and from the N-DRC to the ODAs via the outer–inner dynein linkers[26].

Table 1.

Cryo-EM data collection, refinement and validation statistics

	Composite map of isolated RS1 (EMD-22475, PDB 7JTK)	Composite map of RS2 stalk–IDAc–N-DRC/DMT (EMD-22481, PDB 7JU4)	On-doublet RS1 stalk (EMD-22480, PDB 7JTS)	On-doublet RS1 spokehead (EMD-22482)	On-doublet RS2 spokehead (EMD-22483)	On-doublet RSP1 dimer (EMD-22486)
Data collection and processing						
Magnification	81,000	81,000	81,000	81,000	81,000	81,000
Voltage (kV)	300	300	300	300	300	300
Electron exposure (e⁻/Å²)	60.0	38.9	38.9	38.9	38.9	38.9
Defocus range (μm)	−1.1 to −2.4	−1.0 to −3.5	−1.0 to −3.5	−1.0 to −3.5	−1.0 to −3.5	−1.0 to −3.5
Pixel size (Å)	1.09	1.403	1.403	1.403	1.403	1.403
Symmetry imposed	$C1$	$C1$	$C1$	$C1$	$C1$	$C1$
Initial particle images (no.)	2,320,543	202,168 [*]	202,168	202,168	202,168	202,168
Final particle images (no.)	221,836	202,168	143,514	95,932	121,492	49,714
Map resolution (Å)	3.2 - 3.7 [†]	3.4 - 4.1	6.1	5.3	4.6	6.3
FSC threshold	0.143	0.143	0.143	0.143	0.143	0.143
Refinement						
Map sharpening B factor (Å²)	−74 to −32 [†]	−139 to −50	−100	−127	−160	−300
Model composition						
Non-hydrogen atoms	72,807	133,504	6,801	-	-	-
Protein residues	9,516	17,032	1,377	-	-	-
Ligands	4 PO₄	14 GDP / 14 GTP / 14 Mg / 1 ATP	-	-	-	-
B factors (Å²)						
Protein	30.8	61.56	17.62	-	-	-
Ligand	50	51.4	-	-	-	-
R.m.s. deviations						
Bond lengths (Å)	0.005	0.005	0.005	-	-	-
Bond angles (°)	1.058	1.048	1.364	-	-	-
Validation						
MolProbity score	1.69	2.07	2	-	-	-
Clashscore	9.18	14.77	9.26	-	-	-
Poor rotamers (%)	0.51	0.04	0	-	-	-
Ramachandran plot						
Favored (%)	96.78	94.2	91.44	-	-	-
Allowed (%)	3.22	5.8	8.04	-	-	-
Disallowed (%)	0	0	0.52	-	-	-

[*] Refers to the number of 96-nm particles.

[†]Ranges correspond to the values of the individual maps prior to merging to form the composite map.